

Joint Communication and Sensing in RIS-enabled mmWave Networks

Lu Wang, Luis F. Abanto-Leon, and Arash Asadi

Abstract

Empowering cellular networks with augmented sensing capabilities is one of the key research areas in 6G communication systems. Recently, we have witnessed a plethora of efforts to devise solutions that integrate sensing capabilities into communication systems, i.e., joint communication and sensing (JCAS). However, most prior works do not consider the impact of reconfigurable intelligent surfaces (RISs) on JCAS systems, especially at millimeter-wave (mmWave) bands. Given that RISs are expected to become an integral part of cellular systems, it is important to investigate their potential in cellular networks beyond communication goals. In this paper, we study mmWave orthogonal frequency-division multiplexing (OFDM) JCAS systems in the presence of RISs. Specifically, we jointly design the hybrid beamforming and RIS phase shifts to guarantee the sensing functionalities via minimizing a chordal-distance metric, subject to signal-to-interference-plus-noise (SINR) and power constraints. The non-convexity of the investigated problem poses a challenge which we address by proposing a solution based on the penalty method and manifold-based alternating direction method of multipliers (ADMM). Simulation results demonstrate that under various settings both sensing and communication experience improved performance when the RIS is adequately designed. In addition, we discuss the tradeoff between sensing and communication.

Index Terms

JCAS, RIS, OFDM, hybrid beamforming, ADMM, manifold optimization

This work was supported by the project Deutsche Forschungsgemeinschaft (DFG) mmCell under Grant 416765679.

Lu Wang, Luis F. Abanto-Leon, and Arash Asadi are with the Department of Computer Science, Technische Universität Darmstadt, Darmstadt 64289, Germany (e-mail: lwang@wise.tu-darmstadt.de; labanto@seemoo.tu-darmstadt.de; aasadi@wise.tu-darmstadt.de).

I. INTRODUCTION

Joint communication and sensing (JCAS) is one of the core research areas in 6G communication systems. By integrating sensing and communication into one physical unity, JCAS adds a new dimension to network intelligence allowing the users and the operators to obtain/sense information from their surrounding environment [1]. This opens up new possibilities for emerging use-cases involving autonomous or assisted navigation and smart home monitoring. However, this integration is a challenging task, in particular at millimeter-wave (mmWave) frequencies where both base station and users rely on highly directional beamforming. In such situations, we need effective solutions for beamforming not only towards the communication end-point but also the sensed target. Furthermore, JCAS becomes even more challenging in the presence of reconfigurable intelligent surfaces (RISs), which are expected to be deployed massively in 6G communication systems. Particularly, the beamforming design in such scenarios should simultaneously consider the mobile users for communication, the targets for sensing, and the phase configuration of RIS.

A. *Prior Works*

To date, the majority of existing works either focused on JCAS [2]–[18] or RISs [19]–[34]. Hence, we first provide an overview of the state of the art on JCAS and RIS respectively, and then review the limited number of works that address JCAS in the presence of RIS.

JCAS. The existing works in JCAS mostly focused on the waveform design [2]–[5], performance tradeoff optimization [6]–[8], communication-assisted sensing [9], [10] and sensing-assisted communication [11], [12]. In recent years, we have observed more works on the design of JCAS at mmWave bands [11]–[18]. Specifically, in [13]–[15], the authors designed hybrid beamformers all through formulating the tradeoff problem between communication and sensing. Besides, the works in [16], [17] designed the hybrid beamforming for multi-carrier JCAS systems. The works in [11], [12], [18] considered beam training, tracking, and prediction in JCAS systems at mmWave bands.

RIS. Intelligent surfaces have been extensively studied from a communication perspective in the past few years [19] with different design goals including sum-rate maximization [20], [21], power minimization [22], [23], energy efficiency maximization [24], [25], and minimal user fairness maximization [26], and in various scenarios including non-orthogonal multiple access network [27], mobile edge computing network [28], and simultaneous wireless information and

TABLE I
RIS-ASSISTED JCAS RELATED WORKS.

| Ref. | System | | Spectrum | OFDM | Beamforming | RIS | |
|------------|-------------|---------------|-----------|------|---------------------|---------------|---------|
| | Multi-users | Multi-targets | | | | Communication | Sensing |
| [35] | ✗ | ✗ | Sub-6 GHz | ✗ | ✗ | ✗ | ✓ |
| [36] | ✓ | ✓ | Sub-6 GHz | ✗ | ✗ | ✓ | ✗ |
| [37] | ✓ | ✓ | Sub-6 GHz | ✗ | ✗ | ✓ | ✗ |
| [38] | ✗ | ✗ | Sub-6 GHz | ✗ | Digital beamforming | ✓ | ✓ |
| [39] | ✗ | ✗ | Sub-6 GHz | ✗ | Digital beamforming | ✓ | ✓ |
| [40] | ✗ | ✗ | mmWave | ✗ | ✗ | ✓ | ✓ |
| [41] | ✓ | ✗ | Sub-6 GHz | ✓ | Digital beamforming | ✓ | ✓ |
| [42] | ✓ | ✗ | Sub-6 GHz | ✗ | ✗ | ✓ | ✓ |
| [43] | ✓ | ✓ | Terahertz | ✗ | Digital beamforming | ✓ | ✓ |
| This paper | ✓ | ✓ | mmWave | ✓ | Hybrid beamforming | ✓ | ✓ |

power transfer system [29]. There also exists a small set of works on exploiting RIS for sensing but mostly focusing on detection and estimation aspects, such as improving target detection probability [30], target parameters estimation [31], Cramer-Rao lower bound optimization [32] and human gesture recognition [33], [34]. All these foregoing applications of RIS in either communication system or sensing system demonstrate the potential of exploiting RIS in JCAS system.

RIS-assisted JCAS. So far, only a handful of works have investigated JCAS in the presence of RISs [35]–[43]. The works in [35]–[37] considered JCAS-enabled base stations (BSs) but the RIS usage was limited to sensing/localization [35] or communication only [36], [37]. The authors in [38]–[40] designed JCAS systems leveraging the usage of RISs for scenarios with a single user and a single target. The authors of [41] realized RIS-assisted JCAS to investigate the tradeoff between sensing signal-to-interference-plus-noise-ratio (SINR) and communication SINR in scenarios with multiple users. In [42], the transmit waveform and phase shifts were jointly designed in order to satisfy the SINR constraints, which was solved by the alternative direction method of multipliers (ADMM) framework and majorization minimization algorithm. The work in [43] jointly designed the beamforming and phase shifts in the terahertz band with the proposed primal-dual proximal policy optimization method. However, their solution is only applicable to fully-digital beamforming which is difficult to realize at higher frequencies as it

needs a dedicated radio frequency (RF) chain for each antenna element. Table I summarizes the state of the art in RIS-assisted JCAS research. *We highlight that none of the aforementioned works has considered the RIS-assisted JCAS design in mmWave orthogonal frequency-division multiplexing (OFDM) systems, which requires the joint optimization of the RIS phase shifts and hybrid beamforming, while taking into account the multi-carrier nature of the system.* In the next sub-section, we discuss our motivation and contributions.

B. Contributions

In this article, we investigate RIS-assisted OFDM JCAS systems in mmWave cellular networks. Aligned with 5G new radio (NR) specifications, we adopt OFDM as the physical waveform of the system, and consider multiple targets and users which experience different channel conditions on each sub-carrier [44]. To improve the performance of communication and sensing, we need to jointly design the hybrid beamforming and RIS elements, thus guaranteeing (i) communication for the mobile users and (ii) sensing of the targets. To realize the aforementioned goals, we formulate an optimization problem which proves to be non-convex, in particular, due to variable coupling, non-convex SINR constraints, and constant-modulus constraints that are inherent to the RIS elements and hybrid beamforming. Therefore, we propose a manifold-based ADMM algorithm which is capable of coping with the complex structure of the formulated problem. In the following, we summarize our contributions in more detail.

- To the best of our knowledge, this is the first effort towards modeling an OFDM JCAS cellular system at mmWave bands in the presence of RISs. To guarantee the sensing performance, we minimize a chordal-distance metric as the objective function, which we define as the difference between the transmit covariance matrices across all sub-carriers and a reference sensing matrix. In particular, the reference sensing matrix is designed to have main lobes in the directions of the targets. As constraints, we incorporate SINR requirements per user per sub-carrier to guarantee the communication performance. In addition, we consider a transmit power constraint and constant-modulus phase shifts due to the hybrid beamforming and RIS.
- To solve the non-convex problem, we first introduce an auxiliary variable to decouple the RF beamformer and baseband beamformer. Then, we leverage the penalty method to deal with the non-convex SINR constraints. A manifold-based ADMM framework is adopted to

tackle the newly transformed problem, where each variable is optimized in an alternating and iterative manner until convergence.

- We evaluate our proposal via extensive simulations under different parameters. Specifically, we assess its performance by analyzing the convergence, the sensing performance, and the communication performance. The sensing performance is evaluated via the beam pattern. The communication performance is evaluated via computing the feasibility ratio of SINR values above the predefined threshold. Furthermore, four benchmark schemes are compared with the proposed scheme, namely the fully-digital beamforming with RIS scheme, the fully-digital beamforming without RIS scheme, the hybrid beamforming without RIS scheme, and the hybrid beamforming with random RIS phase shifts scheme. The results show that our proposal improves both sensing and communication performances with the assistance of RIS. The tradeoff between sensing and communication is also illustrated via comparing the SINR feasibility ratio and average SINR results versus the beam pattern mean square error (MSE) produced by the reference sensing matrix and the covariance matrices of designed beamformers.

C. Organization and Notation

The remainder of this paper is organized as follows: Section II introduces the system model of the RIS-assisted mmWave OFDM JCAS system followed by the problem formulation. Section III presents the proposed solution. In Section V, simulation results and discussion are provided. Finally, conclusions are summarized in Section VI.

Regarding notations, bold-face uppercase and lowercase, \mathbf{A} and \mathbf{a} , represent matrices and vectors, respectively. $\mathbb{E}\{\cdot\}$, $\text{tr}(\cdot)$, and $\mathcal{O}(\cdot)$ stand for the expectation, the trace of a square matrix, and the computational complexity order. $(\cdot)^T$ and $(\cdot)^H$ denote the transpose and the Hermitian transpose of a matrix or vector. $|\cdot|$ and $\|\cdot\|_F$ represent the absolute value of a scalar and the Frobenius norm of a matrix, respectively. The symbols \otimes , \odot , $\langle \cdot, \cdot \rangle$ represent the Kronecker product, the Hadamard product, and the Euclidean inner product, respectively. ∇ denotes the Euclidean gradient. $\text{blkdiag}(\cdot)$ and $\text{diag}(\cdot)$ are functions to form a block diagonal or diagonal matrix with the elements in (\cdot) , respectively. \mathbb{C} and \mathbb{R} denote the complex and real numbers, respectively.

II. SYSTEM MODEL AND PROBLEM FORMULATION

We consider an OFDM JCAS system operating at mmWave frequency, where an RIS is deployed to assist communication and sensing, as shown in Fig. 1. The BS is equipped with N_t antennas, which are spaced by half wavelength thus forming a uniform linear array (ULA). In addition, the BS has a small number of RF chains which is denoted by N_{RF} , such that $N_{RF} \ll N_t$. The BS serves K single-antenna user equipments (UEs) and senses M targets, simultaneously. The RIS is configured as a rectangular uniform planar array (UPA) with R reflecting elements. The number of sub-carriers is denoted as N_c . The interval between adjacent sub-carriers is Δf .

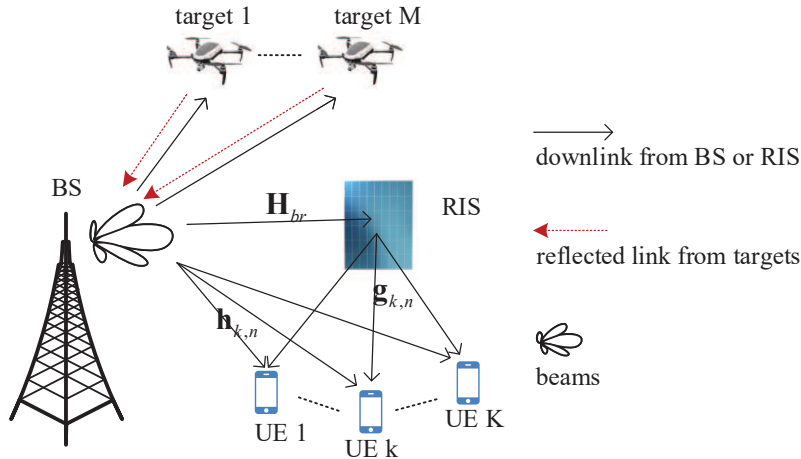


Fig. 1. Overview of the RIS-assisted JCAS system at mmWave frequency.

A. Transmission Signals and Hybrid Beamforming

Let $\mathbf{X} = [\mathbf{X}_1^T, \dots, \mathbf{X}_n^T, \dots, \mathbf{X}_{N_c}^T]^T \in \mathbb{C}^{N_c K \times L}$ denote the transmit symbols from the BS to all the K UEs on all the N_c sub-carriers, where $\mathbf{X}_n = [\mathbf{x}_{1,n}, \dots, \mathbf{x}_{k,n}, \dots, \mathbf{x}_{K,n}]^T \in \mathbb{C}^{K \times L}$ stands for the transmit symbols for all the K UEs on the sub-carrier $n \in \mathcal{N}_c$. Besides, L represents the length of symbols. $\mathbf{x}_{k,n} \in \mathbb{C}^{L \times 1}$ refers to the data for the UE k on the sub-carrier n , satisfying $\mathbb{E}\{\mathbf{x}_{k,n} \mathbf{x}_{k,n}^H\} = \mathbf{I}_L$.

Hybrid beamforming consists of digital beamforming (a.k.a. baseband precoding) and analog beamforming (a.k.a. RF analog processing). The baseband digital beamforming is sub-carrier

dependent whereas RF analog beamforming is identical for all the sub-carriers [45]. The transmit symbols are first digitally processed by the precoding matrix \mathbf{W}^{BB} in frequency domain as

$$\mathbf{X}^{BB} = \mathbf{W}^{BB}\mathbf{X} = [(\mathbf{X}_1^{BB})^T, \dots, (\mathbf{X}_{N_c}^{BB})^T]^T \in \mathbb{C}^{N_c N_{RF} \times L}, \quad (1)$$

where $\mathbf{W}^{BB} = \text{blkdiag}(\mathbf{W}_1^{BB}, \dots, \mathbf{W}_n^{BB}, \dots, \mathbf{W}_{N_c}^{BB}) \in \mathbb{C}^{N_c N_{RF} \times N_c K}$ collects the precoding matrices for all the K UEs on all the N_c sub-carriers, $\mathbf{W}_n^{BB} = [\mathbf{w}_{1,n}^{BB}, \dots, \mathbf{w}_{k,n}^{BB}, \dots, \mathbf{w}_{K,n}^{BB}] \in \mathbb{C}^{N_{RF} \times K}$ represents the baseband precoding matrix for all the K UEs on the sub-carrier n , and $\mathbf{w}_{k,n}^{BB} \in \mathbb{C}^{N_{RF} \times 1}$ is the baseband precoding vector for the UE k on the sub-carrier n . Besides, $\mathbf{X}_n^{BB} = \mathbf{W}_n^{BB}\mathbf{X}_n \in \mathbb{C}^{N_{RF} \times L}$ is the precoded signal after digital beamforming for all the K UEs on the sub-carrier n .

Then, the inverse discrete Fourier transform (IDFT) operation is applied to \mathbf{X}^{BB} thus yielding

$$\mathbf{X}^{ID} = (\mathbf{F}^H \otimes \mathbf{I}_{N_{RF}})\mathbf{W}^{BB}\mathbf{X} \in \mathbb{C}^{N_c N_{RF} \times L} = [(\mathbf{X}_1^{ID})^T, \dots, (\mathbf{X}_{N_c}^{ID})^T]^T \in \mathbb{C}^{N_c N_{RF} \times L}, \quad (2)$$

where $\mathbf{F} \in \mathbb{C}^{N_c \times N_c}$ is the discrete Fourier transform (DFT) matrix. For the (n, n') -th element of \mathbf{F} ($n \in \mathcal{N}_c, n' \in \mathcal{N}_c$), it is calculated as follows

$$F_{n,n'} = \frac{1}{\sqrt{N_c}} e^{-j\frac{2\pi}{N_c}(n-1)(n'-1)}. \quad (3)$$

Therefore, $(\mathbf{F}^H \otimes \mathbf{I}_{N_{RF}}) \in \mathbb{C}^{N_c N_{RF} \times N_c N_{RF}}$ in (2) corresponds to a N_c -point IDFT for all the N_{RF} RF chains. In addition, $\mathbf{X}_n^{ID} = (\mathbf{f}_n^H \otimes \mathbf{I}_{N_{RF}})\mathbf{W}^{BB}\mathbf{X} \in \mathbb{C}^{N_{RF} \times L}$ in (2) is the transmitted signal after the IDFT operation for all the N_{RF} RF chains on the sub-carrier n , where $\mathbf{f}_n \in \mathbb{C}^{N_c \times 1}$ is the n -th column of \mathbf{F} , corresponding to the DFT operation on the sub-carrier n .

Within the OFDM structure, the cyclic prefix is then added at the beginning of each OFDM symbol to deal with inter-symbol interference. Afterwards, the signals are up-converted, and RF analog beamforming is performed by the RF precoder $\mathbf{W}^{RF} = \text{blkdiag}(\mathbf{W}_1^{RF}, \dots, \mathbf{W}_{N_c}^{RF}) \in \mathbb{C}^{N_c N_t \times N_c N_{RF}}$ in the time domain. Since the RF precoder is the same for all sub-carriers, we use $\tilde{\mathbf{W}}^{RF}$ to denote it, such that $\mathbf{W}_1^{RF} = \mathbf{W}_2^{RF} = \dots = \mathbf{W}_{N_c}^{RF} = \tilde{\mathbf{W}}^{RF} \in \mathbb{C}^{N_t \times N_{RF}}$. Therefore, the transmitted signal of all the K UEs on all the N_c sub-carriers after RF analog beamforming can be expressed as follows

$$\mathbf{X}^{RF} = \mathbf{W}^{RF}(\mathbf{F}^H \otimes \mathbf{I}_{N_{RF}})\mathbf{W}^{BB}\mathbf{X} \in \mathbb{C}^{N_c N_t \times L} = [(\mathbf{X}_1^{RF})^T, \dots, (\mathbf{X}_{N_c}^{RF})^T]^T \in \mathbb{C}^{N_c N_t \times L}, \quad (4)$$

where $\mathbf{X}_n^{RF} = \tilde{\mathbf{W}}^{RF}(\mathbf{f}_n^H \otimes \mathbf{I}_{N_{RF}})\mathbf{W}^{BB}\mathbf{X} \in \mathbb{C}^{N_t \times L}$ is the signal for all the K UEs on the n -th sub-carrier after analog beamforming.

B. RIS Reflection and Channel Model

The signals transmitted from the BS arrive at the UEs by direct transmission and indirect reflection via RIS. Regarding the reflected path from the RIS, let $\theta_r \in [0, 2\pi)$ and $\beta_r \in [0, 1]$ denote the phase shift and the reflection amplitude imposed by the r -th reflection element on the incident signals, respectively. Let $\Theta = \text{diag}(\beta_1 e^{j\theta_1}, \dots, \beta_R e^{j\theta_R})$ group the phase shifts and amplitudes of all RIS elements. Due to the high path loss at mmWave band, it is assumed that the power of the signals reflected two or more times by RIS is negligible and thus ignored [46].

The channels from the BS to all the K UEs on all the N_c sub-carriers, from the BS to the RIS on all the N_c sub-carriers, and from the RIS to all the K UEs on all the N_c sub-carriers are denoted by $\mathbf{H} = \text{blkdiag}(\mathbf{H}_1, \dots, \mathbf{H}_n, \dots, \mathbf{H}_{N_c}) \in \mathbb{C}^{N_c N_t \times N_c K}$, $\mathbf{H}_{br} = \text{blkdiag}(\mathbf{H}_{br,1}, \dots, \mathbf{H}_{br,n}, \dots, \mathbf{H}_{br,N_c}) \in \mathbb{C}^{N_c N_t \times N_c R}$ and $\mathbf{G} = \text{blkdiag}(\mathbf{G}_1, \dots, \mathbf{G}_n, \dots, \mathbf{G}_{N_c}) \in \mathbb{C}^{N_c R \times N_c K}$, respectively. The channel $\mathbf{H}_n = [\mathbf{h}_{1,n}, \dots, \mathbf{h}_{k,n}, \dots, \mathbf{h}_{K,n}] \in \mathbb{C}^{N_t \times K}$ is from the BS to all the K UEs on the sub-carrier n , where $\mathbf{h}_{k,n} \in \mathbb{C}^{N_t \times 1}$ is the channel from the BS to the UE k on the sub-carrier n . The channel $\mathbf{h}_{k,n}$ is modelled as the extended Saleh-Valenzuela model [44], given by:

$$\mathbf{h}_{k,n} = \sqrt{\frac{N_t}{N_{cl} N_p}} \sum_c^{N_{cl}} \sum_p^{N_p} \alpha_{c,p}^{bu} \mathbf{a}_b^H(\phi_{b,c,p}) e^{-j \frac{2\pi \psi_c n}{N_c}}, \quad (5)$$

where between the BS and the UE k , ψ_c is the phase shift of c -th cluster, N_{cl} and N_p represent the number of clusters and scattering paths in each cluster, $\alpha_{c,p}^{bu}$ and $\phi_{b,c,p}$ are the complex gain and the angle of departure (AoD) for the p -th scattering path in the c -th cluster, and $\mathbf{a}_b(\phi_{b,c,p})$ is the transmit array response vector. Given the ULA structure with N_t antennas at the BS, the transmit array response vector is expressed as

$$\mathbf{a}_b(\phi) = \sqrt{\frac{1}{N_t}} [1, e^{j \frac{2\pi}{\lambda} d \cos(\phi)}, \dots, e^{j \frac{2\pi}{\lambda} d (N_t - 1) \cos(\phi)}]^T, \quad (6)$$

where d and λ are the antenna space and wavelength respectively, satisfying the relation $d = \lambda/2$.

Equipped with UPA, the RIS is configured with $R = R_h \times R_v$ elements, where R_h and R_v are the number of elements in horizontal direction and vertical direction, respectively. Denoting $\phi_{r,c,p}$ ($\varphi_{r,c,p}$) as the azimuth (elevation) angle of arrival (AoA) for the p -th scattering path in the c -th cluster, the channel from the BS to the RIS on the sub-carrier n , $\mathbf{H}_{br,n} \in \mathbb{C}^{N_t \times R}$, is given by

$$\mathbf{H}_{br,n} = \sqrt{\frac{N_t R}{N_{cl} N_p}} \sum_c^{N_{cl}} \sum_p^{N_p} \alpha_{c,p}^{br} \mathbf{a}_r(\phi_{r,c,p}, \varphi_{r,c,p}) \mathbf{a}_b^H(\phi_{b,c,p}) e^{-j \frac{2\pi \psi_c n}{N_c}}, \quad (7)$$

where for the p -th scattering path in the c -th cluster, $\alpha_{c,p}^{br}$ is the complex gain, $\mathbf{a}_r(\phi, \varphi) = \mathbf{a}_{rh}(\phi, \varphi) \otimes \mathbf{a}_{rv}(\phi, \varphi)$ is the receive antenna array response at RIS, with

$$\mathbf{a}_{rh}(\phi, \varphi) = \sqrt{\frac{1}{R_h}} [1, e^{j\frac{2\pi}{\lambda}d \sin(\varphi) \cos(\phi)}, \dots, e^{j\frac{2\pi}{\lambda}d(R_h-1) \sin(\varphi) \cos(\phi)}]^T, \quad (8)$$

$$\mathbf{a}_{rv}(\phi, \varphi) = \sqrt{\frac{1}{R_v}} [1, e^{j\frac{2\pi}{\lambda}d \cos(\varphi)}, \dots, e^{j\frac{2\pi}{\lambda}d(R_v-1) \cos(\varphi)}]^T. \quad (9)$$

Similarly, $\mathbf{G}_n = [\mathbf{g}_{1,n}, \dots, \mathbf{g}_{k,n}, \dots, \mathbf{g}_{K,n}] \in \mathbb{C}^{R \times K}$ is the channel from the RIS to all the K UEs on the sub-carrier n , where $\mathbf{g}_{k,n} \in \mathbb{C}^{R \times 1}$ is the channel from the RIS to the UE k on the sub-carrier n , given by

$$\mathbf{g}_{k,n} = \sqrt{\frac{R}{N_{cl}N_p}} \sum_c^{N_{cl}} \sum_p^{N_p} \alpha_{c,p}^{ru} \mathbf{a}_r^H(\phi_{r,c,p}, \varphi_{r,c,p}) e^{-j\frac{2\pi\psi_{cn}}{N_c}}. \quad (10)$$

where $\alpha_{c,p}^{ru}$ is the complex gain of the p -th scattering path in the c -th cluster between RIS and UE k .

We assume that the channel state information (CSI) of all channels involved is perfectly estimated, which can be realized by the current channel estimation techniques [47].

C. Communication Model

At the receiver side, each UE deals with the information extraction individually. The received signals after the OFDM demodulation can be expressed in frequency domain as follows

$$\mathbf{Y} = (\mathbf{H}^T + \mathbf{G}^T \Theta \mathbf{H}_{br}^T) \mathbf{W}^{RF} \mathbf{W}^{BB} \mathbf{X} + \mathbf{N}_c, \quad (11)$$

where \mathbf{N}_c is the complex Gaussian noise with zero mean and variance σ_c^2 . By denoting $(\mathbf{H} + \mathbf{H}_{br} \Theta^T \mathbf{G})$ as $\tilde{\mathbf{H}}$, (11) is recast as

$$\mathbf{Y} = \tilde{\mathbf{H}}^T \mathbf{W}^{RF} \mathbf{W}^{BB} \mathbf{X} + \mathbf{N}_c. \quad (12)$$

Accordingly, the SINR of UE k on the sub-carrier n at the receiver side is given by

$$\gamma_{k,n} = \frac{\left| \tilde{\mathbf{h}}_{k,n} \tilde{\mathbf{W}}^{RF} \mathbf{w}_{k,n}^{BB} \right|^2}{\sum_{i=1, i \neq k}^K \left| \tilde{\mathbf{h}}_{k,n} \tilde{\mathbf{W}}^{RF} \mathbf{w}_{i,n}^{BB} \right|^2 + \sigma_c^2}. \quad (13)$$

where $\tilde{\mathbf{h}}_{k,n}$ is the combined channel for the UE k on the sub-carrier n .

D. Sensing Model

The BS simultaneously senses towards the directions where M targets are located. The corresponding transmit beampattern is calculated as

$$BP = \mathbf{a}'^H(\psi) \mathbf{R}_p \mathbf{a}'(\psi). \quad (14)$$

where $\mathbf{a}'(\psi) = [1, e^{j2\pi d \cos(\psi)}, \dots, e^{j2\pi d(N_t-1) \cos(\psi)}]^T \in \mathbb{C}^{N_t \times 1}$ is the antenna steering vector with detection angle ψ , and $\mathbf{R}_p = \mathbb{E}\{\mathbf{W}^{RF} \mathbf{W}^{BB} \mathbf{X} \mathbf{X}^H (\mathbf{W}^{BB})^H (\mathbf{W}^{RF})^H\} = \mathbf{W}^{RF} \mathbf{W}^{BB} (\mathbf{W}^{BB})^H (\mathbf{W}^{RF})^H$ refers to the covariance matrix of the precoded transmitted signals. Given the antenna steering vector, the design of the covariance matrix \mathbf{R}_p is equivalent to the design of beampattern, which influences the detection performance and parameter estimation performance [48]. Note that the sensing is designed such that RIS is not used for illuminating the targets but is leveraged to improve sensing by increasing the amount of available power for sensing. In the following sections, we explain how the sensing is designed.

E. Problem Formulation

In this paper, we aim to simultaneously optimize the performances of sensing and communication. To guarantee the communication performance, SINR is leveraged as a metric and the SINR of each UE on each sub-carrier is constrained to be not smaller than a predefined threshold. Meanwhile, to improve the sensing performance for either detection or parameter estimation, we optimize the transmit covariance matrix \mathbf{R}_p by matching it with a reference radar transmit covariance matrix. To realize this, we minimize the difference between the transmit covariance matrices and the reference covariance matrix while simultaneously satisfying the transmit power and SINR requirements by jointly designing the hybrid beamforming and RIS phase shifts. Note that when the communication SINR is improved with the assistance of RIS, more transmit power can be saved from communication and utilized for sensing. This aforementioned optimization problem is mathematically formulated as

$$(P1) \quad \min_{\mathbf{W}^{RF}, \mathbf{W}^{BB}, \Theta} \|\mathbf{R}_p - \mathbf{R}_{\text{ref}}\|_F^2 \quad (15a)$$

$$\text{s.t.} \quad \gamma_{k,n} \geq \Gamma_{k,n}, \forall k \in \mathcal{K}, n \in \mathcal{N}_c, \quad (15b)$$

$$\|\mathbf{W}^{RF} \mathbf{W}^{BB}\|_F^2 = P_{\text{max}}, \quad (15c)$$

$$\left| \tilde{\mathbf{W}}^{RF}(i, j) \right| = 1, \forall i \in \mathcal{N}_t, j \in \mathcal{N}_{RF}, \quad (15d)$$

$$\theta_r \in [0, 2\pi), \forall r \in \mathcal{R}. \quad (15e)$$

where \mathbf{R}_{ref} is the reference covariance matrix for all the sub-carriers. For each sub-carrier, the reference covariance matrix is obtained by the method used in [3]. The constraint (15b) guarantees the communication performance by ensuring that the SINR of UE k on the sub-carrier n is not smaller than a predefined minimum SINR requirement $\Gamma_{k,n}$. The constraints (15c) and (15d) are the power allocation for hybrid beamforming over all the sub-carriers, which is supposed to consume all the provided power for better sensing effects [3], making the problem solving more difficult. Assuming the reflection amplitudes of RIS elements are all one, the constraint (15e) is the design of RIS phase shifts.

From the objective function (15a) and the constraints (15b) and (15c), we can observe that all the variables in the problem P1 are coupled with each other, which makes the non-convex problem P1 more difficult to solve. In the next section, we propose a manifold-based ADMM algorithm to tackle the formulated problem.

III. PROPOSED SOLUTION

In this section, we introduce our proposed solution. Considering the difficulty of directly solving the original problem P1, we first transform problem P1 into a more tractable form (i.e., problem P2). Then, a manifold-based ADMM algorithm is proposed to obtain the solution. Details are described in the following.

To make the formulated problem more tractable, we first introduce an auxiliary variable $\mathbf{W} = \mathbf{W}^{RF}\mathbf{W}^{BB} \in \mathbb{C}^{N_c N_t \times N_c K}$ to decouple the RF analog beamformer \mathbf{W}^{RF} and baseband digital beamformer \mathbf{W}^{BB} . Then the problem P1 becomes the following problem P2.

$$(P2) \quad \min_{\mathbf{W}^{RF}, \mathbf{W}^{BB}, \mathbf{w}, \Theta} \|\mathbf{W}\mathbf{W}^H - \mathbf{R}_{\text{ref}}\|_{\text{F}}^2 \quad (16a)$$

$$\text{s.t.} \quad \mathbf{W} = \mathbf{W}^{RF}\mathbf{W}^{BB}, \quad (16b)$$

$$\frac{|\tilde{\mathbf{h}}_{k,n}\mathbf{w}_{k,n}|^2}{\sum_{i=1, i \neq k}^K |\tilde{\mathbf{h}}_{k,n}\mathbf{w}_{i,n}|^2 + \sigma_c^2} \geq \Gamma_{k,n}, \forall k \in \mathcal{K}, n \in \mathcal{N}_c, \quad (16c)$$

$$\|\mathbf{W}\|_{\text{F}}^2 = P_{\text{max}}, \quad (16d)$$

$$|\mathbf{W}_n^{RF}(i, j)| = 1, \forall i \in \mathcal{N}_t, j \in \mathcal{N}_{RF}, \quad (16e)$$

$$\theta_r \in [0, 2\pi), \forall r \in \mathcal{R}. \quad (16f)$$

Leveraging the equality constraint (16b), we apply the ADMM framework to tackle the problem P2. The augmented Lagrangian function of the problem P2 is calculated as

$$\begin{aligned} L &= \|\mathbf{W}\mathbf{W}^H - \mathbf{R}_{\text{ref}}\|_{\text{F}}^2 + \text{tr}(\Lambda^H(\mathbf{W} - \mathbf{W}^{RF}\mathbf{W}^{BB})) + \frac{\rho_1}{2} \|\mathbf{W} - \mathbf{W}^{RF}\mathbf{W}^{BB}\|_{\text{F}}^2 \\ &= \|\mathbf{W}\mathbf{W}^H - \mathbf{R}_{\text{ref}}\|_{\text{F}}^2 + \frac{\rho_1}{2} \left\| \mathbf{W} + \frac{\Lambda}{\rho_1} - \mathbf{W}^{RF}\mathbf{W}^{BB} \right\|_{\text{F}}^2. \end{aligned} \quad (17)$$

where $\Lambda \in \mathbb{C}^{N_c N_t \times N_c K}$ and $\rho_1 > 0$ are the Lagrangian multipliers and the penalty parameter, respectively. Then, all the variables and Lagrangian multipliers $\{\mathbf{W}, \mathbf{W}^{RF}, \mathbf{W}^{BB}, \Theta, \Lambda\}$ update as follows:

A. Update of Auxiliary Variable

Given $\{\mathbf{W}^{RF}, \mathbf{W}^{BB}, \Theta, \Lambda\}$, the sub-problem for the auxiliary variable \mathbf{W} is expressed as

$$\mathbf{W}^{(t)} = \arg \min_{\mathbf{W}} L(\mathbf{W}, \mathbf{W}^{RF(t-1)}, \mathbf{W}^{BB(t-1)}, \Theta^{(t-1)}, \Lambda^{(t-1)}) \quad (18a)$$

$$\text{s.t.} \quad \frac{\left| \tilde{\mathbf{h}}_{k,n} \mathbf{w}_{k,n} \right|^2}{\sum_{i=1, i \neq k}^K \left| \tilde{\mathbf{h}}_{k,n} \mathbf{w}_{i,n} \right|^2 + \sigma_c^2} \geq \Gamma_{k,n}, \forall k \in \mathcal{K}, n \in \mathcal{N}_c, \quad (18b)$$

$$\|\mathbf{W}\|_{\text{F}}^2 = P_{\text{max}}. \quad (18c)$$

The existence of the SINR constraint (18b) makes the problem (18) still challenging to be tackled. Therefore, the SINR inequality constraint is further integrated into the objective function by using the penalty method [29]. This means if the solution satisfies the SINR constraint, it is equivalent to the original problem (18), otherwise the penalty is given to the unsuitable solution. The new problem with the SINR penalty is expressed as follows

$$\text{(P2.1)} \min_{\mathbf{W}} \left\{ \|\mathbf{W}\mathbf{W}^H - \mathbf{R}_{\text{ref}}\|_{\text{F}}^2 + \frac{\rho_1}{2} \left\| \mathbf{W} + \frac{\Lambda}{\rho_1} - \mathbf{W}^{RF}\mathbf{W}^{BB} \right\|_{\text{F}}^2 + \rho_2 \sum_{k=1}^K \sum_{n=1}^{N_c} P_{k,n}^{\mathbf{W}} \right\} \quad (19a)$$

$$\text{s.t.} \quad \|\mathbf{W}\|_{\text{F}}^2 = P_{\text{max}}. \quad (19b)$$

where $P_{k,n}^{\mathbf{W}} = (\min\{\gamma_{k,n} - \Gamma_{k,n}, 0\})^2$, and ρ_2 is the penalty parameter for SINR constraint, which usually updates from a small value to a large value.

Denoting $\mathbf{B}_{k,n} = \tilde{\mathbf{h}}_{k,n} (\tilde{\mathbf{h}}_{k,n})^H$ and $\mathbf{F}_{k,n} = \mathbf{w}_{k,n} (\mathbf{w}_{k,n})^H$, we have the following transformation

$$\sum_{k=1}^K \sum_{n=1}^{N_c} (\gamma_{k,n} - \Gamma_{k,n})^2 = \sum_{k=1}^K \sum_{n=1}^{N_c} \left(\frac{\text{tr}(\mathbf{B}_{k,n} \mathbf{F}_{k,n})}{\text{tr} \left(\mathbf{B}_{k,n} \sum_{i=1, i \neq k}^K \mathbf{F}_{i,n} \right) + \sigma_c^2} - \Gamma_{k,n} \right)^2. \quad (20)$$

From the perspective of optimization, (20) is equivalent to

$$\sum_{k=1}^K \sum_{n=1}^{N_c} (\gamma_{k,n} - \Gamma_{k,n})^2 = \sum_{k=1}^K \sum_{n=1}^{N_c} (\gamma'_{k,n} - \sigma_c^2 \Gamma_{k,n})^2, \quad (21)$$

where $\gamma'_{k,n}$ is given by

$$\gamma'_{k,n} = (1 + \Gamma_{k,n}) \text{tr}(\mathbf{B}_{k,n} \mathbf{F}_{k,n}) - \Gamma_{k,n} \text{tr} \left(\mathbf{B}_{k,n} \sum_{i=1}^K \mathbf{F}_{i,n} \right). \quad (22)$$

Therefore, $P_{k,n}^{\mathbf{W}}$ is equivalent to

$$P_{k,n}^{\mathbf{W}} = (\min \{ \gamma'_{k,n} - \sigma_c^2 \Gamma_{k,n}, 0 \})^2. \quad (23)$$

After the SINR constraint transformation, the only constraint for power (19b) is equivalent to $\|\mathbf{W}\|_{\text{F}} = \sqrt{P_{\max}}$. The problem P2.1 then can be regarded as a non-constraint problem over manifold, where the feasible set is a $N_c N_t \times N_c K - 1$ dimension complex hypersphere. Therefore, the problem P2.1 can be rewritten as follows

$$\min_{\mathbf{W} \in \mathcal{S}_{\mathbf{W}}} f_{\mathbf{W}} = \left\{ \|\mathbf{W}\mathbf{W}^{\text{H}} - \mathbf{R}_{\text{ref}}\|_{\text{F}}^2 + \frac{\rho_1}{2} \left\| \mathbf{W} + \frac{\Lambda}{\rho_1} - \mathbf{W}^{RF} \mathbf{W}^{BB} \right\|_{\text{F}}^2 + \rho_2 \sum_{k=1}^K \sum_{n=1}^{N_c} P_{k,n}^{\mathbf{W}} \right\}, \quad (24)$$

where $\mathcal{S}_{\mathbf{W}} = \{ \mathbf{W} \in \mathbb{C}^{N_c N_t \times N_c K} \mid \|\mathbf{W}\|_{\text{F}} = \sqrt{P_{\max}} \}$ represents the complex hypersphere manifold with the radius of $\sqrt{P_{\max}}$. To efficiently solve the problem (24), we leverage a Riemannian Conjugate Gradient (RCG)-based algorithm, which can realize the near-optimal solution under a low complexity [49], [50].

Firstly, we define the tangent space over the manifold $\mathcal{S}_{\mathbf{W}}$ as $T_{\mathbf{W}}\mathcal{S}_{\mathbf{W}}$, which is the space consisting of all the tangent vectors over $\mathcal{S}_{\mathbf{W}}$, namely

$$T_{\mathbf{W}}\mathcal{S}_{\mathbf{W}} = \{ \mathbf{T} \in \mathbb{C}^{N_c N_t \times N_c K} \mid \text{Re} \{ \mathbf{T} \odot \mathbf{W}^* \} = \mathbf{0} \}. \quad (25)$$

Then the Riemannian gradient of $\mathcal{S}_{\mathbf{W}}$ at point \mathbf{W} is $\text{grad}(f_{\mathbf{W}})$, which is obtained by projecting the Euclidean gradient of $f_{\mathbf{W}}$ on the tangent space $T_{\mathbf{W}}\mathcal{S}_{\mathbf{W}}$, namely

$$\text{grad}(f_{\mathbf{W}}) = \text{Proj}_{\mathbf{W}}(f_{\mathbf{W}}) = \nabla f_{\mathbf{W}} - \text{Re} \{ \nabla f_{\mathbf{W}} \odot \mathbf{W}^* \} \odot \mathbf{W}. \quad (26)$$

where the Euclidean gradient $\nabla f_{\mathbf{W}}$ of $f_{\mathbf{W}}$ is given by

$$\nabla f_{\mathbf{W}} = 4(\mathbf{W}\mathbf{W}^{\text{H}} - \mathbf{R}_{\text{ref}}) \mathbf{W} + \rho_1 \left(\mathbf{W} + \frac{\Lambda}{\rho_1} - \mathbf{W}^{RF} \mathbf{W}^{BB} \right) + 4\rho_2 \sum_{k=1}^K \sum_{n=1}^{N_c} \nabla P_{k,n}^{\mathbf{W}}. \quad (27)$$

where $\nabla P_{k,n}^{\mathbf{W}}$ is given by (28), and $\mathbf{e}_{k,n} \in \mathbb{R}^{K \times 1}$ has all-zero entries except for its k -th entry, which is equal to 1.

$$\nabla P_{k,n}^{\mathbf{W}} = \begin{cases} 0, & \text{if } (\gamma'_{k,n} - \sigma_c^2 \Gamma_{k,n}) \geq 0, \\ (\gamma'_{k,n} - \sigma_c^2 \Gamma_{k,n}) \mathbf{B}_{k,n} ((1 + \Gamma_{k,n}) \mathbf{w}_{k,n} \mathbf{e}_{k,n}^H - \Gamma_{k,n} \mathbf{W}_n), & \text{otherwise.} \end{cases} \quad (28)$$

Under RCG-based algorithm, the auxiliary variable updates according to the descent direction and the step size in each iteration. For the q -th iteration, the search direction $\mathbf{\Pi}_{\mathbf{W}}^{(q)}$ is determined by the Riemannian gradient $\text{grad} \left(f_{\mathbf{W}}^{(q)}(\mathbf{W}) \right)$ and the $(q-1)$ -th search direction $\mathbf{\Pi}_{\mathbf{W}}^{(q-1)}$, namely

$$\mathbf{\Pi}_{\mathbf{W}}^{(q)} = -\text{grad} \left(f_{\mathbf{W}}^{(q)} \right) + \varpi_{\mathbf{W}}^{(q-1)} \text{Proj}_{\mathbf{W}}^{(q)} \left(\mathbf{\Pi}_{\mathbf{W}}^{(q-1)} \right). \quad (29)$$

where $\varpi_{\mathbf{W}}^{(q)}$ is obtained by the Polak-Ribière formula [50], expressed as

$$\varpi_{\mathbf{W}}^{(q)} = \frac{\left\langle \text{grad} \left(f_{\mathbf{W}}^{(q)} \right), \text{grad} \left(f_{\mathbf{W}}^{(q)} \right) - \text{Proj}_{\mathbf{W}}^{(q-1)} \left(f_{\mathbf{W}}^{(q-1)} \right) \right\rangle}{\left\langle \text{grad} \left(f_{\mathbf{W}}^{(q-1)} \right), \text{grad} \left(f_{\mathbf{W}}^{(q-1)} \right) \right\rangle}. \quad (30)$$

where $\langle \cdot, \cdot \rangle$ is the Euclidean inner product operation.

For the q -th iteration, the step size $\mu_{\mathbf{W}}^{(q)}$ is obtained by the Armijo line search rule [50]. With the descent direction $\mathbf{\Pi}_{\mathbf{W}}^{(q)}$ and the step size $\mu_{\mathbf{W}}^{(q)}$ at the q -th iteration, the auxiliary variable is updated at the $(q+1)$ -th iteration by the *retraction* over the manifold $\mathcal{S}_{\mathbf{W}}$, namely

$$\mathbf{W}^{(q+1)} = \mathcal{R}_{\mathbf{W}}^{(q)} \left(\mu_{\mathbf{W}}^{(q)} \mathbf{\Pi}_{\mathbf{W}}^{(q)} \right) = \frac{\left(\mathbf{W}^{(q)} + \mu_{\mathbf{W}}^{(q)} \mathbf{\Pi}_{\mathbf{W}}^{(q)} \right)}{\left\| \mathbf{W}^{(q)} + \mu_{\mathbf{W}}^{(q)} \mathbf{\Pi}_{\mathbf{W}}^{(q)} \right\|_{\mathbb{F}}}. \quad (31)$$

where $\mathcal{R}_{\mathbf{W}}(\mu_{\mathbf{W}} \mathbf{\Pi}_{\mathbf{W}}) = (\mathbf{W} + \mu_{\mathbf{W}} \mathbf{\Pi}_{\mathbf{W}}) / \|\mathbf{W} + \mu_{\mathbf{W}} \mathbf{\Pi}_{\mathbf{W}}\|_{\mathbb{F}}$ is the retraction operator, mapping a vector from the tangent space to the manifold $\mathcal{S}_{\mathbf{W}}$.

The whole procedure of the RCG-based algorithm for obtaining the auxiliary variable \mathbf{W} is concluded as Algorithm 1.

B. Update of RF Beamforming Variable

Given $\{\mathbf{W}, \mathbf{W}^{BB}, \Theta, \mathbf{\Lambda}\}$, the sub-problem with respect to the RF beamformer \mathbf{W}^{RF} is expressed as

$$\mathbf{W}^{RF(t)} = \arg \min_{\mathbf{W}^{RF}} L(\mathbf{W}^{(t)}, \mathbf{W}^{RF}, \mathbf{W}^{BB(t-1)}, \Theta^{(t-1)}, \mathbf{\Lambda}^{(t-1)}) \quad (32a)$$

$$\text{s.t.} \quad \left| \tilde{\mathbf{W}}^{RF}(i, j) \right| = 1, \forall i \in \mathcal{N}_t, j \in \mathcal{N}_{RF}. \quad (32b)$$

Algorithm 1 The RCG-based algorithm for the auxiliary variable

- 1: **Input:** $\mathbf{W}^{RF(t-1)}$, $\mathbf{W}^{BB(t-1)}$, $\Theta^{(t-1)}$, $\Lambda^{(t-1)}$, ρ_1 , Q_{\max} , and $\varepsilon_{\mathbf{W}}$.
 - 2: **Initialize:** Set $\mathbf{W} \in \mathcal{S}_{\mathbf{W}}$ randomly, $q = 1$.
 - 3: **repeat**
 - 4: Obtain the stepsize $\mu_{\mathbf{W}}^{(q)}$ by the Armijo rule.
 - 5: Obtain the Polak-Ribière parameter $\varpi_{\mathbf{W}}^{(q)}$ by (30).
 - 6: Obtain the search direction $\Pi_{\mathbf{W}}^{(q)}$ by (29).
 - 7: Update the auxiliary variable $\mathbf{W}^{(q)}$ by (31).
 - 8: Update $q = q + 1$
 - 9: **until** $q < Q_{\max}$ or $\left\| \text{grad} \left(f_{\mathbf{W}}^{(q)} \right) \right\|_{\text{F}} \leq \varepsilon_{\mathbf{W}}$
 - 10: **Output:** the solved auxiliary variable $\mathbf{W}^{(t)} = \mathbf{W}^{(q)}$.
-

Omitting the unrelated terms, the RF analog beamforming problem becomes

$$\min_{\mathbf{W}^{RF}} \frac{\rho_1}{2} \left\| \mathbf{W} + \frac{\Lambda}{\rho_1} - \mathbf{W}^{RF} \mathbf{W}^{BB} \right\|_{\text{F}}^2 \quad (33a)$$

$$\text{s.t.} \quad \left| \tilde{\mathbf{W}}^{RF}(i, j) \right| = 1, \forall i \in \mathcal{N}_t, j \in \mathcal{N}_{RF}. \quad (33b)$$

Since the RF analog beamformer is identical for each sub-carrier, we can reformulate the objective function in (33) as follows

$$\min_{\tilde{\mathbf{W}}^{RF}} \frac{\rho_1}{2} \sum_{n=1}^{N_c} \left\| \mathbf{W}_n + \frac{\Lambda_n}{\rho_1} - \tilde{\mathbf{W}}^{RF} \mathbf{W}_n^{BB} \right\|_{\text{F}}^2 \quad (34a)$$

$$\text{s.t.} \quad \left| \tilde{\mathbf{W}}^{RF}(i, j) \right| = 1, \forall i \in \mathcal{N}_t, j \in \mathcal{N}_{RF}. \quad (34b)$$

Similarly, the problem (34) can also be regarded as a problem without constraint over the complex circle manifold $\mathcal{S}_{\tilde{\mathbf{W}}^{RF}} = \left\{ \tilde{\mathbf{W}}^{RF} \in \mathbb{C}^{N_t \times N_{RF}} \mid \left| \tilde{\mathbf{W}}^{RF}(i, j) \right| = 1 \right\}$. Therefore, the RF analog beamforming sub-problem can also be solved by the RCG-based algorithm, with the procedure similar to Algorithm 1. The Euclidean gradient of $\tilde{\mathbf{W}}^{RF}$ is calculated as

$$\nabla f_{\tilde{\mathbf{W}}^{RF}} = \rho_1 \sum_{n=1}^{N_c} \left(\tilde{\mathbf{W}}^{RF} \mathbf{W}_n^{BB} (\mathbf{W}_n^{BB})^{\text{H}} - \left(\mathbf{W}_n + \frac{\Lambda_n}{\rho_1} \right) (\mathbf{W}_n^{BB})^{\text{H}} \right), \quad (35)$$

where the feasible set is a $N_t \times K - 1$ dimension complex hypersphere. The other similar procedure of manifold optimization process is omitted due to limited space.

C. Update of Baseband Beamforming Variable

Given $\{\mathbf{W}, \mathbf{W}^{RF}, \Theta, \Lambda\}$, the baseband digital beamformer \mathbf{W}^{BB} can be optimized by solving the following sub-problem:

$$\mathbf{W}^{BB(t)} = \arg \min_{\mathbf{W}^{BB}} L(\mathbf{W}^{(t)}, \mathbf{W}^{RF(t)}, \mathbf{W}^{BB}, \Theta^{(t-1)}, \Lambda^{(t-1)}). \quad (36)$$

After omitting the unrelated parameters, the baseband digital beamforming problem becomes

$$\min_{\mathbf{W}^{BB}} \frac{\rho_1}{2} \left\| \mathbf{W} + \frac{\eta}{\rho_1} - \mathbf{W}^{RF} \mathbf{W}^{BB} \right\|_F^2. \quad (37)$$

With no constraints in (37), the closed form of \mathbf{W}^{BB} can be obtained as follows

$$(\mathbf{W}^{BB})^* = \left((\mathbf{W}^{RF})^H \mathbf{W}^{RF} \right)^{-1} (\mathbf{W}^{RF})^H \left(\mathbf{W} + \frac{\Lambda}{\rho_1} \right). \quad (38)$$

D. Update of Phase Shift Variable

Given $\{\mathbf{W}, \mathbf{W}^{RF}, \mathbf{W}^{BB}, \Lambda\}$, the problem for the phase shift variable Θ is expressed as

$$\Theta^{(t)} = \arg \min_{\Theta} L(\mathbf{W}^{(t)}, \mathbf{W}^{RF(t)}, \mathbf{W}^{BB(t)}, \Theta, \Lambda^{(t-1)}). \quad (39)$$

To decouple the phase shift variable with all the other parameters, the transformation is first performed as $(\mathbf{h}_{k,n}^T + \mathbf{g}_{k,n}^T \Theta \mathbf{h}_{br,n}^T) \tilde{\mathbf{W}}^{RF} \mathbf{w}_{k,n}^{BB} = b_{k,n} + \mathbf{v}^H \mathbf{a}_{k,n}$, where $\mathbf{v} = [e^{j\theta_1}, \dots, e^{j\theta_r}, \dots, e^{j\theta_R}]^H$. $v_r = e^{j\theta_r}, \forall r$. $\mathbf{a}_{k,n} = \text{diag}(\mathbf{g}_{k,n}^T) \mathbf{h}_{br,n}^T \tilde{\mathbf{W}}^{RF} \mathbf{w}_{k,n}^{BB}$ and $b_{k,n} = \mathbf{h}_{k,n}^T \tilde{\mathbf{W}}^{RF} \mathbf{w}_{k,n}^{BB}$. Omitting the unrelated parameters, the passive beamforming design problem turns into the following problem P3, given by

$$(P3) \text{ find } \mathbf{v} \quad (40a)$$

$$\text{s.t. } \frac{|b_{k,n} + \mathbf{v}^H \mathbf{a}_{k,n}|^2}{\sum_{i=1, i \neq k}^K |b_{i,n} + \mathbf{v}^H \mathbf{a}_{i,n}|^2 + \sigma_c^2} \geq \Gamma_{k,n}, \forall k \in \mathcal{K}, n \in \mathcal{N}_c, \quad (40b)$$

$$|v_r| = 1, \forall r \in \mathcal{R}, \quad (40c)$$

where $b_{i,n} = \mathbf{h}_{k,n}^H \tilde{\mathbf{W}}^{RF} \mathbf{w}_{i,n}^{BB}$ and $\mathbf{a}_{i,n} = \text{diag}(\mathbf{g}_{k,n}^H) \mathbf{h}_{br,n}^H \tilde{\mathbf{W}}^{RF} \mathbf{w}_{i,n}^{BB}$. The SINR constraint (40b) is still a challenging part for solving \mathbf{v} . To ensure a near-optimal and faster solution, we first transform the SINR constraint and then utilize the similar RCG-based algorithm as Algorithm 1. The SINR constraint (40b) can be equivalently transformed as follows

$$\left((1 + \Gamma_{k,n}) |b_{k,n} + \mathbf{v}^H \mathbf{a}_{k,n}|^2 - \Gamma_{k,n} \sum_{i=1}^K |b_{i,n} + \mathbf{v}^H \mathbf{a}_{i,n}|^2 - \sigma_c^2 \Gamma_{k,n} \right) \geq 0, \forall k \in \mathcal{K}, n \in \mathcal{N}_c. \quad (41)$$

Utilizing the penalty method, the SINR constraint (41) is integrated into the objective function, after which the problem P3 turns into the problem P3.1, given by

$$(P3.1) \quad \min_{\mathbf{v}} f_{\mathbf{v}} = \rho_3 \sum_{k=1}^K \sum_{n=1}^{N_c} P_{k,n}(\mathbf{v}) \quad (42a)$$

$$\text{s.t.} \quad |v_r| = 1, \forall r \in \mathcal{R}. \quad (42b)$$

where $P_{k,n}(\mathbf{v})$ is given by

$$P_{k,n}(\mathbf{v}) = \left(\min \left\{ \left((1 + \Gamma_{k,n}) |b_{k,n} + \mathbf{v}^H \mathbf{a}_{k,n}|^2 - \Gamma_{k,n} \sum_{i=1}^K |b_{i,n} + \mathbf{v}^H \mathbf{a}_{i,n}|^2 - \sigma_c^2 \Gamma_{k,n} \right), 0 \right\} \right)^2. \quad (43)$$

Then, the problem P3.1 can be regarded as a problem without constraint over the complex circle manifold $\mathcal{S}_{\mathbf{v}} = \{\mathbf{v} \in \mathbb{C}^{R \times 1} \mid |v_r| = 1, \forall r \in \mathcal{R}\}$, which can be solved by the RCG-based algorithm, similar to the Algorithm 1. The Euclidean gradient of (42a) is given by

$$\nabla f_{\mathbf{v}} = \rho_3 \sum_{k=1}^K \sum_{n=1}^{N_c} \nabla P_{k,n}(\mathbf{v}). \quad (44)$$

where $\nabla P_{k,n}(\mathbf{v})$ is derived as (45). Other similar optimization procedure is omitted.

$$\nabla P_{k,n}(\mathbf{v}) = \begin{cases} 0, & \text{if } \left((1 + \Gamma_{k,n}) |b_{k,n} + \mathbf{v}^H \mathbf{a}_{k,n}|^2 - \Gamma_{k,n} \sum_{i=1}^K |b_{i,n} + \mathbf{v}^H \mathbf{a}_{i,n}|^2 - \sigma_c^2 \Gamma_{k,n} \right) \geq 0, \\ 4 \left((1 + \Gamma_{k,n}) |b_{k,n} + \mathbf{v}^H \mathbf{a}_{k,n}|^2 - \Gamma_{k,n} \sum_{i=1}^K |b_{i,n} + \mathbf{v}^H \mathbf{a}_{i,n}|^2 - \sigma_c^2 \Gamma_{k,n} \right) \times \\ \quad \left((1 + \Gamma_{k,n}) (\mathbf{a}_{k,n} \mathbf{a}_{k,n}^H \mathbf{v} + \mathbf{a}_{k,n} b_{k,n}^H) - \Gamma_{k,n} \sum_{i=1}^K (\mathbf{a}_{i,n} \mathbf{a}_{i,n}^H \mathbf{v} + \mathbf{a}_{i,n} b_{i,n}^H) \right) & \text{otherwise.} \end{cases} \quad (45)$$

E. Update of Lagrangian Multiplier

The update rule of the Lagrangian multipliers Λ is expressed as

$$\Lambda^{(t)} = \Lambda^{(t-1)} + \rho_1 (\mathbf{W}^{(t)} - \mathbf{W}^{RF(t)} \mathbf{W}^{BB(t)}). \quad (46)$$

In conclusion, all the variables and Lagrangian multipliers $\{\mathbf{W}, \mathbf{W}^{RF}, \mathbf{W}^{BB}, \Theta, \Lambda\}$ are alternately iterated under ADMM framework until the convergence is reached. The entire manifold-based ADMM algorithm for solving problem P1 is summarized as Algorithm 2.

Algorithm 2 Manifold-based ADMM algorithm for solving problem P1

- 1: **Input:** \mathbf{W} , \mathbf{W}^{RF} , \mathbf{W}^{BB} , Θ , Λ , ρ_1 , ρ_2 , ρ_3 , and I_{ADMM} .
 - 2: **Initialize:** Set \mathbf{W} , \mathbf{W}^{RF} , \mathbf{W}^{BB} randomly, $\rho_1 = 0.1$, $\rho_2 = 1$, $\rho_3 = 0.1$ and $\Lambda = \mathbf{0}$.
 - 3: **repeat**
 - 4: Update the auxiliary variable \mathbf{W} by Algorithm 1.
 - 5: Update the RF beamforming variable \mathbf{W}^{RF} by RCG-based algorithm.
 - 6: Update the baseband beamforming variable \mathbf{W}^{BB} by (38).
 - 7: Update the phase shift variable \mathbf{v} by RCG-based algorithm.
 - 8: Update the Lagrangian multipliers Λ by (46).
 - 9: Update the penalty parameters as $\min\{2\rho_1, 100\}$, $\min\{10\rho_2, 1000\}$ and $\min\{2\rho_3, 100\}$.
 - 10: **until** convergence
 - 11: **Output:** the solved variables $\{\mathbf{W}, \mathbf{W}^{RF}, \mathbf{W}^{BB}, \Theta\}$.
-

F. Complexity Analysis

In this section, we analyse the computational complexity of the proposed algorithm, where the complexity mainly depends on obtaining $\mathbf{W}, \mathbf{W}^{RF}, \mathbf{W}^{BB}$ and Θ . Among these variables, the complexity of the manifold-based solutions for $\mathbf{W}, \mathbf{W}^{RF}$ and Θ dominantly depends on calculating the Euclidean gradient, which are $\mathcal{O}(I_{\mathbf{W}}(N_c^3 N_t^2 K + N_c^3 N_t N_{RF} K + N_c N_t^2 K^2))$, $\mathcal{O}(I_{\mathbf{W}^{RF}}(N_c N_t N_{RF} K))$ and $\mathcal{O}(I_{\Theta} K R^2)$, respectively. $I_{\mathbf{W}}$, $I_{\mathbf{W}^{RF}}$ and I_{Θ} are the number of iterations for solving $\mathbf{W}, \mathbf{W}^{RF}$ and Θ , respectively. The complexity of calculating the closed-form solution for \mathbf{W}^{BB} is $\mathcal{O}(N_c^3 (N_{RF}^2 N_t + N_{RF}^3 + N_{RF} N_t K))$. Therefore, the total computational complexity of the proposed algorithm is $\mathcal{O}(I_{ADMM}(I_{\mathbf{W}}(N_c^3 N_t^2 K + N_c^3 N_t N_{RF} K + N_c N_t^2 K^2) + I_{\mathbf{W}^{RF}}(N_c N_t N_{RF} K) + I_{\Theta} K R^2 + N_c^3 (N_{RF}^2 N_t + N_{RF}^3 + N_{RF} N_t K)))$, where I_{ADMM} is the number of iterations for ADMM algorithm.

IV. NUMERICAL RESULTS

In this section, we evaluate our proposed manifold-based ADMM algorithm via numerical simulation from four aspects. Firstly, the convergence of the proposed algorithm is tested by observing the variation of the objective function in problem P1. Then, to validate the sensing performance, the designed beampattern obtained from the proposed algorithm is compared against the reference beampattern, and the beampatterns from other four schemes. Furthermore,

to measure the impact of different parameters on the system performance, we analyse the SINR feasibility ratio (defined as the percentage of satisfying SINR requirements by all UEs over all sub-carriers) for communication and beampattern for sensing under different values of number of UEs, number of RF chains, RIS size, minimum SINR requirements, and ratio of transmit power to noise power (denoted as χ). Finally, the performance tradeoff between sensing and communication is analyzed.

To better assess the performance of our proposed scheme, we compare our solution against four other schemes, namely,

- **Manifold-based fully-digital beamforming with RIS (denoted as ‘FDB with RIS’)**: In this comparative scheme, we replace the hybrid beamforming with the digital beamforming to see the upper bound performance of the proposed system framework, where the variables of digital beamformer and phase shifts are alternatingly iterated via the same penalty method and manifold optimization.
- **Manifold-based fully-digital beamforming without RIS (denoted as ‘FDB w/o RIS’)**: The difference between this scheme and the ‘FDB with RIS’ scheme is that RIS is not deployed in the network of this scheme.
- **Manifold-based hybrid beamforming without RIS (denoted as ‘HB w/o RIS’)**: Unlike in the proposed scheme, here we assume that RIS is not deployed in the network. The hybrid beamforming utilizes the same solution as the proposed scheme.
- **Manifold-based hybrid beamforming with random RIS (denoted as ‘HB with rnd RIS’)**: In this comparative scheme, the RIS is configured with random phase shifts while the optimization of hybrid beamforming is the same as the proposed scheme.

For the **simulation setup** of the considered RIS-assisted mmWave OFDM JCAS system, we assume that the BS serves multiple UEs varying from $K = 2$ to $K = 12$ and three sensing targets ($M = 3$) located in the directions $[40^\circ, 90^\circ, 140^\circ]$. Configured with ULA, BS has $N_t = 64$ antennas and can provide $P_{\max} = 30$ dBm transmit power. Equipped with UPA, RIS is a rectangular RIS with fixed number of columns $R_h = 5$ and varying number of rows $R_v = 5/10/15/20/25/30/35/40$ in different scenarios. The system works at center frequency $f_c = 41$ GHz [51] with $N_c = 8$ sub-carriers. The number of RF chains N_{RF} varies from 2 to 24 for different scenarios. The channels are modeled as the extended Saleh-Valenzuela model as introduced in Section II-B, with $N_{cl} = 8$ clusters and $N_p = 10$ scattering paths for each cluster.

TABLE II
SIMULATION PARAMETERS.

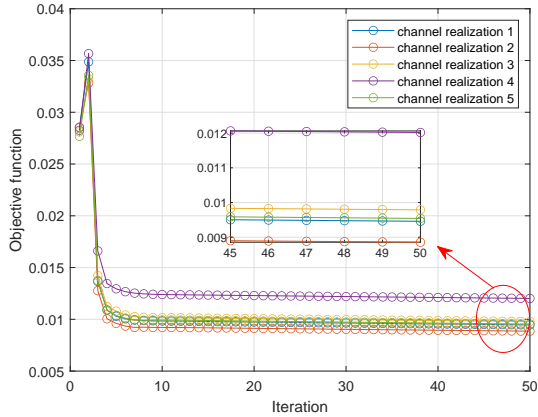
| Notation | Explanation | Value | Notation | Explanation | Value |
|------------|------------------------|-----------------------------------|----------------------------|---|--------------------------|
| N_t | number of antennas | 64 | N_p | number of paths per cluster | 10 |
| N_{RF} | number of RF chains | 2-16 | R_h | number of horizontal RIS elements | 5 |
| N_c | number of sub-carriers | 8 | R_v | number of vertical RIS elements | 5:5:40 |
| f_c | center frequency | 41 GHz | χ | ratio of transmit power over noise power | 51-66 dB |
| Δf | sub-carrier interval | 120 KHz | $\Gamma_{n,k}$ | SINR threshold of user k on sub-carrier n | 6-14 dB |
| K | number of users | 4-12 | Q_{\max} | maximal iterations for manifold solution | 10000 |
| M | number of targets | 3 | $\varepsilon_{\mathbf{W}}$ | accuracy for convergence | 0.001 |
| - | location of targets | $[40^\circ, 90^\circ, 140^\circ]$ | ρ_1 | penalty parameter of ADMM problem | $\min\{2\rho_1, 100\}$ |
| P_{\max} | maximal power of BS | 30 dBm | ρ_2 | penalty parameter of SINR constraint for \mathbf{W} | $\min\{10\rho_2, 1000\}$ |
| N_{cl} | number of clusters | 8 | ρ_3 | penalty parameter of SINR constraint for \mathbf{v} | $\min\{2\rho_3, 100\}$ |

The aforementioned parameters and other important parameters are concluded in Table II.

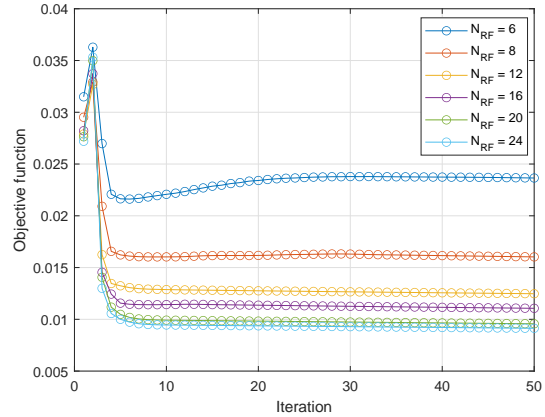
Regarding the **initialization**, we initialize all the variables \mathbf{W} , \mathbf{W}^{RF} , \mathbf{W}^{BB} and Θ with random values. The penalty parameters ρ_1 , ρ_2 and ρ_3 are initialized as 0.1, 1, 0.1, respectively. The Lagrangian multiplier matrix Λ is initialized as a zero matrix $\mathbf{0}$.

A. Convergence Performance

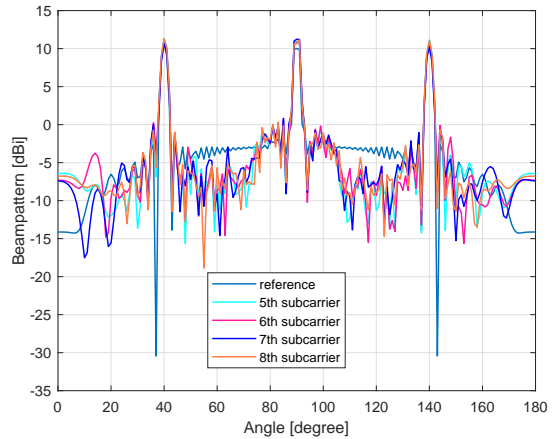
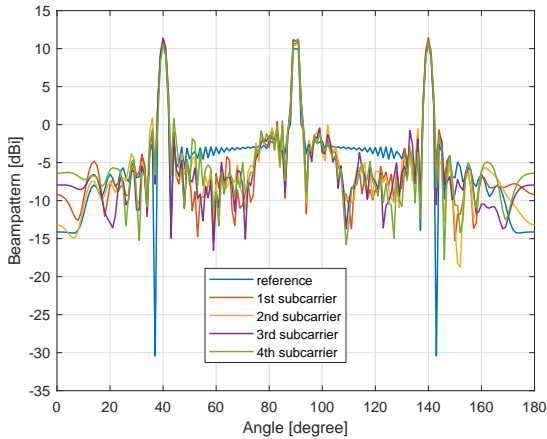
In this sub-section, we evaluate the convergence performance of the proposed algorithm. In Fig. 2, we observe that the objective function, namely the squared error (in the Frobenius norm sense) between the designed and reference covariance matrices, converges fast and approximates to zero under different channel realizations and the number of RF chains. In particular, the errors in Fig. 2(a) achieved by the proposed algorithm under different channel realizations are all around 0.01, i.e., 1% of the transmit power used in this scenario, thus confirming the stability of the solution. Besides, it can be observed from Fig. 2(b) that when the number of RF chains N_{RF} increases, the objective function converges to a smaller value, indicating that the squared error can be decreased by adjusting parameters, e.g. N_{RF} . Therefore, via simulations, we have shown that the proposed algorithm converges.



(a) Convergence under different channel realizations



(b) Convergence under varying number of RF chains

Fig. 2. Convergence of the manifold-based ADMM algorithm ($K = 4$, $R = 100$, $\chi = 60$ dB, $\Gamma_{n,k} = 10$ dB)Fig. 3. Beampattern of each sub-carrier for sensing ($N_{RF} = 16$, $K = 4$, $R = 100$, $\chi = 60$ dB, $\Gamma_{n,k} = 10$ dB)

B. Beampattern Performance

In this sub-section, we illustrate the beampattern performance obtained by the proposed algorithm, and compare it with the reference beampattern and the other four comparative schemes. Fig. 3 shows the designed beampatterns across all the 8 sub-carriers. The legend ‘reference’ represents the beampattern obtained from the reference covariance sensing matrix, which is identical for all sub-carriers. We observe that the designed beampatterns obtained by our proposed algorithm match the reference beampattern, which have main lobes in the directions of interest, thus confirming that the sensing requirements are satisfied.

In Fig. 4, the beampatterns obtained from different schemes are compared, where all the

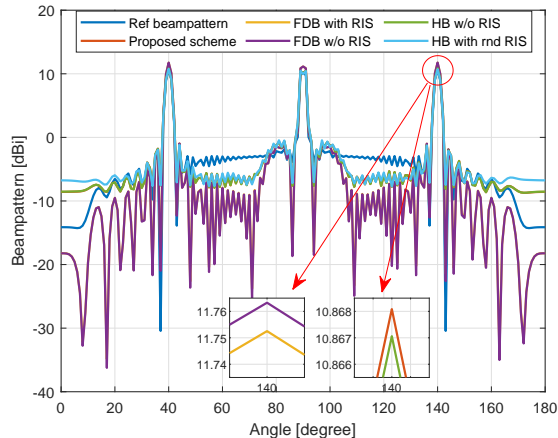


Fig. 4. Beam patterns under different schemes ($K = 4, R = 100, \chi = 63$ dB, $\Gamma_{n,k} = 10$ dB, $N_{RF} = 64$ for fully-digital beamforming, $N_{RF} = 16$ for hybrid beamforming)

beam pattern results are averaged over all sub-carriers. It can be observed that the two fully-digital beamforming schemes ('FDB with RIS', 'FDB w/o RIS') have higher main lobes and lower side lobes than the three hybrid beamforming schemes (proposed scheme, 'HB w/o RIS', and 'HB with rnd RIS'), with around -6.43 dB beam pattern MSE. This is reached at the cost of consuming $N_{RF} = N_t = 64$ RF chains, which is much more than the number of RF chains $N_{RF} = 16$ in hybrid beamforming. Besides, the beam patterns obtained by the schemes with RIS are slightly better than those without RIS or with random RIS. For instance, the beam pattern MSE between our proposed scheme and 'HB with rnd RIS' scheme is -23.15 dB.

C. System Performance under Varying Parameters

In this section, we evaluate the impact of different parameters on the system performance (SINR feasibility ratio for communication, and beam pattern for sensing) under varying number of UEs, number of RF chains, number of RIS elements, minimum SINR requirements, and the ratio of transmit power to noise power $\chi = P_{\max}/\sigma_c^2$. Regarding the comparison of different beam patterns obtained by different schemes, we also conduct experiments for beam patterns under varying parameters for each scheme. The observation of the beam pattern relation among different schemes is consistent with the result shown in Fig. 4. Therefore, in this sub-section, we omit the beam pattern comparison results of different schemes due to the limited space.

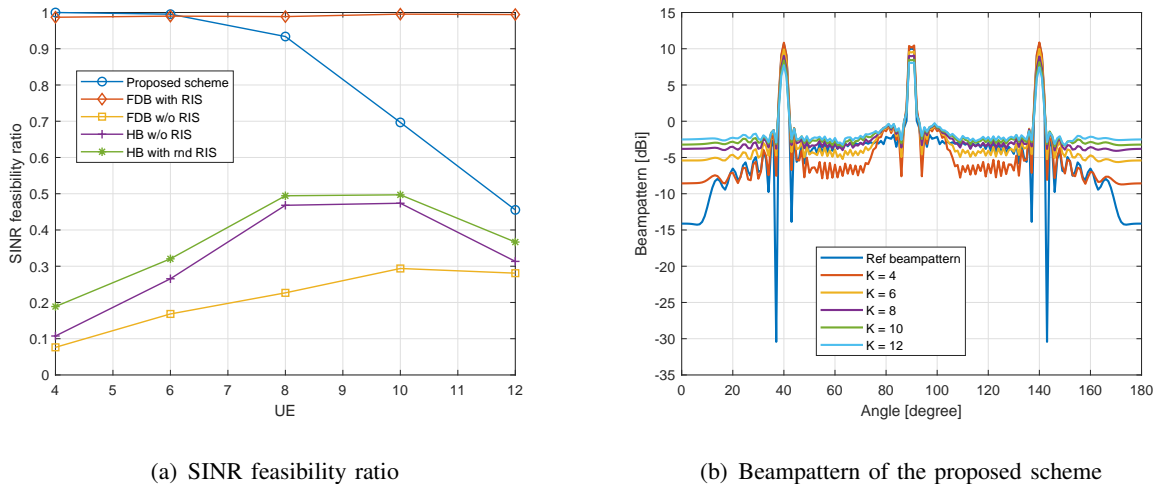


Fig. 5. SINR feasibility ratio and beampattern under varying number of UEs ($N_{RF} = 16$, $R = 100$, $\chi = 63$ dB, $\Gamma_{n,k} = 10$ dB)

1) *Impact of number of UEs on Performance:* Fig. 5 shows the SINR feasibility ratio and beampattern under the varying number of UEs. In the proposed scheme, when the number of UEs increases, the SINR feasibility ratio generally decreases while the beampattern performance becomes worse (lower main lobes and higher side lobes). This is because when the number of UEs increases, the multi-user interference on each sub-carrier increases. With the provision of the same transmit power, it becomes more difficult to satisfy the SINR constraints for all the UEs on all the sub-carriers. Therefore, to meet the UEs' SINR requirements, more transmit power is allocated to UEs to compensate for this multi-user interference. This results in that less power is left for optimizing sensing beampatterns, thus obtaining worse beampatterns under more UEs. Besides, the SINR feasibility ratio of the proposed scheme is better than 'FDB w/o RIS' scheme, 'HB w/o RIS' scheme and 'HB with rnd RIS' scheme with at least 24.19% improvement, demonstrating that the existence of RIS improves the system performance. Furthermore, the 'FDB with RIS' scheme has the best SINR feasibility ratio compared to three hybrid beamforming schemes and 'FDB w/o RIS' scheme. This is realized at the cost of requiring a large number of $N_{RF} = N_t = 64$ RF chains and with the assistance of RIS.

2) *Impact of number of RF chains on Performance:* Fig. 6 demonstrates the influence of RF chains on the system performance. The fully digital beamforming schemes utilize fixed $N_{RF} = N_t$ RF chains. Therefore, we only compare schemes exploiting hybrid beamforming. It can be observed from Fig. 6(a) that when the number of RF chains is equal to the number of UEs, all the schemes have poor SINR (SINR feasibility ratio is less than 0.3), due to the low

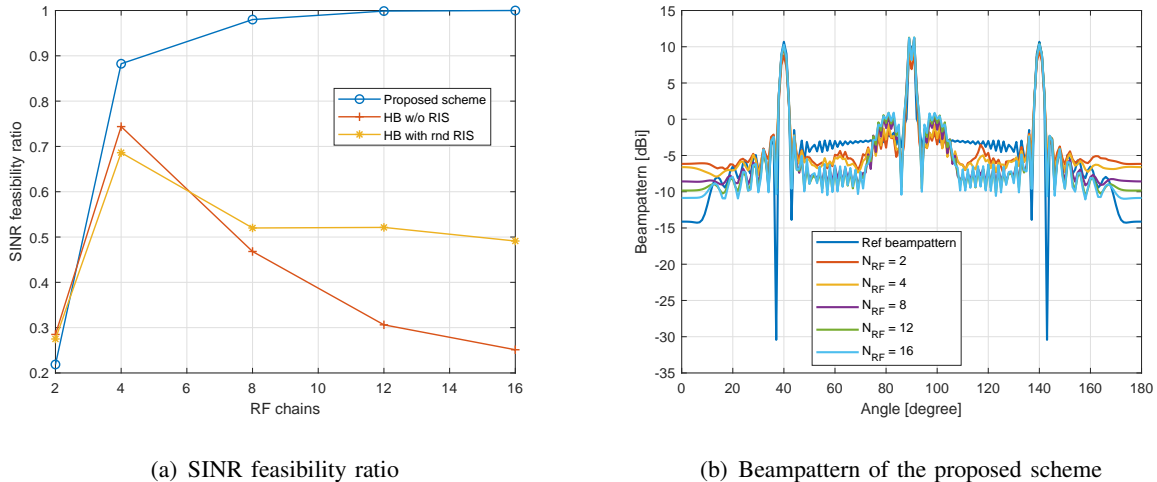
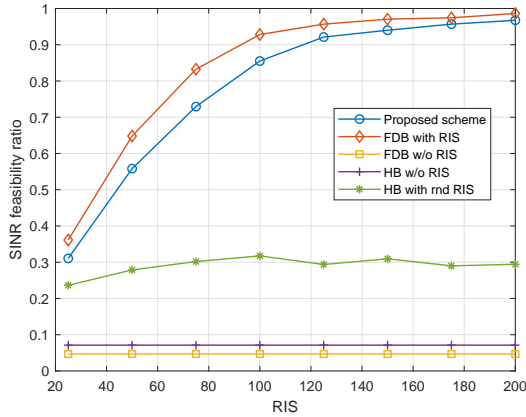


Fig. 6. SINR feasibility ratio and beampattern under varying number of RF chains ($K = 2$, $R = 100$, $\chi = 60$ dB, $\Gamma_{n,k}=10$ dB)

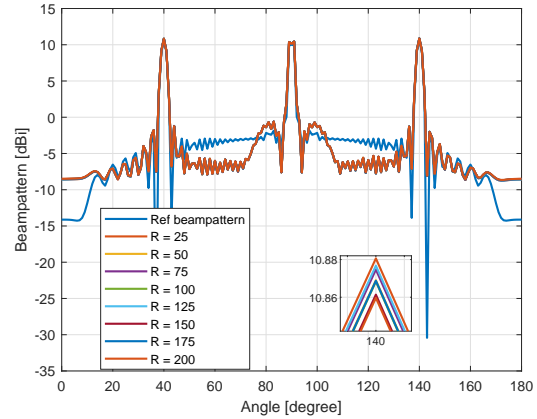
number of RF chains. When the number of RF chains is larger than the number of UEs, the SINR feasibility ratio of the proposed scheme goes beyond 0.88. However, the SINR feasibility ratio of ‘HB w/o RIS’ scheme and ‘HB with rnd RIS’ scheme is inferior to our proposed scheme for at least 18.56%, due to the lack of RIS assistance. In addition, as shown in Fig. 6(b), increasing the number of RF chains improves the sensing beampattern performance (higher main lobes and lower side lobes), which has the same conclusion proved by the converging result in Fig. 2(b).

3) *Impact of number of RIS elements on Performance:* Fig. 7 illustrates the SINR feasibility ratio and beampattern versus the number of RIS elements. It can be observed that for our proposed scheme and ‘FDB with RIS’ scheme, the SINR feasibility ratio improves as the RIS size becomes larger. In contrast, the SINR feasibility ratio in schemes with random RIS phase shifts or without RIS assistance reduces at least from 24.12% (when RIS elements $R = 25$) to 69.57% (when RIS elements $R = 200$) compared to the proposed scheme. The SINR feasibility ratio under ‘HB with rnd RIS’ scheme does not show regular pattern when the number of RIS elements varies due to the random RIS phase configuration. Moreover, the beampatterns under different RIS sizes remain similar. This is because the increasing RIS size assists the network to obtain a higher SINR feasibility ratio, which saves more power from communication to sensing, thus guaranteeing the beampattern performance. Therefore, the existence of RIS improves the system performance and more RIS elements bring better performance improvement.

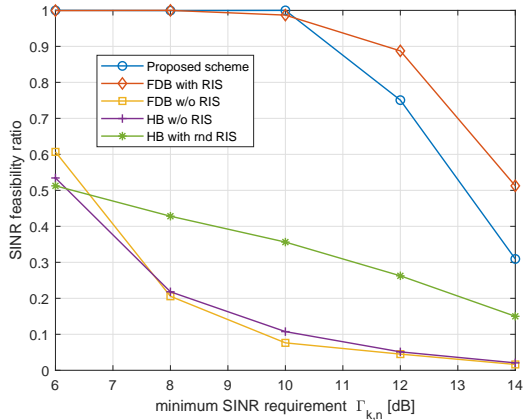
4) *Impact under varying minimum SINR requirements on Performance:* In Fig. 8, the influence of minimum SINR requirements on the sensing and communication performances is shown. We



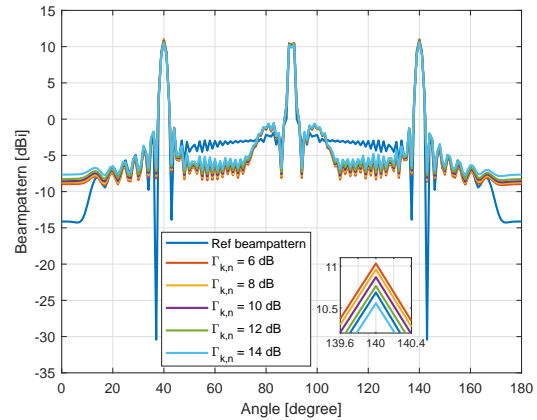
(a) SINR feasibility ratio



(b) Beampattern of the proposed scheme

Fig. 7. SINR feasibility ratio and beampattern under varying RIS sizes ($N_{RF} = 16$, $K = 4$, $\chi = 60$ dB, $\Gamma_{n,k} = 10$ dB)

(a) SINR feasibility ratio



(b) Beampattern of the proposed scheme

Fig. 8. SINR feasibility ratio and beampattern under varying SINR requirements ($N_{RF} = 16$, $K = 4$, $R = 100$, $\chi = 63$ dB)

can observe that our proposal and ‘FDB with RIS’ scheme can reach a feasible solution as long as the minimum required SINR threshold $\Gamma_{n,k}$ is below 10 dB. Beyond this threshold, we can use other measures, e.g. improving the transmit power or utilizing more RIS elements to reach a feasible solution. Besides, the SINR performance of our proposal and ‘FDB with RIS’ scheme is generally much better than the other three schemes, at least improving 39.31% from SINR feasibility ratio 0.6069 to 1 (when $\Gamma_{n,k} = 6$ dB). In addition, the beampattern becomes worse (lower main lobes and higher side lobes) when the minimum SINR requirement increases, as is shown in Fig. 8(b). This stems from that more transmit power is consumed to support the

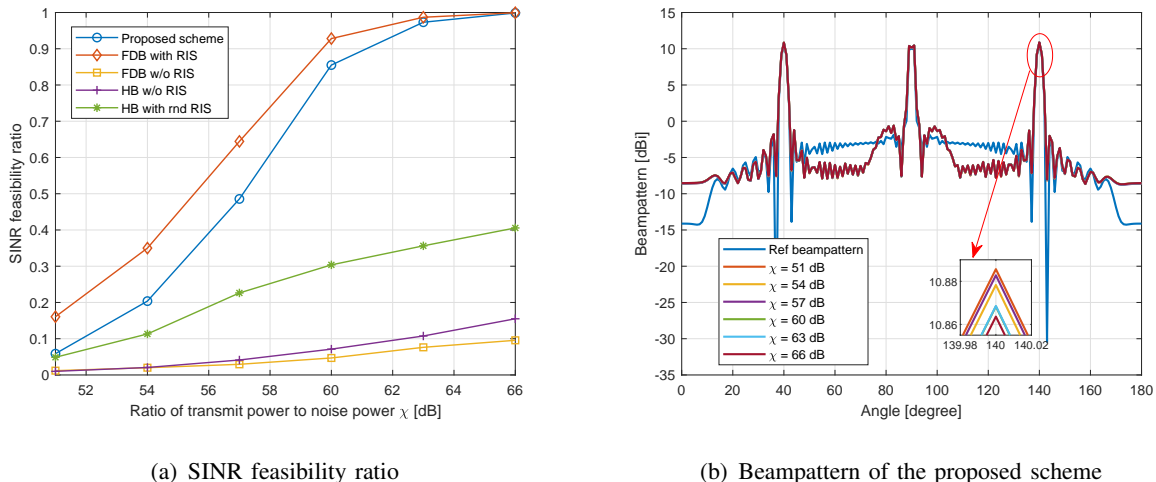


Fig. 9. SINR feasibility ratio and beampattern under varying χ ($N_{RF} = 16, K = 4, R = 100, \Gamma_{n,k} = 10$ dB)

higher SINR requirements, leaving less transmit power for sensing.

5) *Impact of ratio of transmit power to noise power on Performance:* Fig. 9 illustrates the impact of the ratio of transmit power to noise power χ on the system performance. It can be observed that a higher χ results in a higher SINR feasibility ratio, i.e. higher SINR communicating UEs, under all schemes. This is because with a fixed transmit power, the noise power becomes smaller under a higher χ , which makes the SINR requirements easier to be satisfied. Besides, the SINR feasibility ratio of our proposed scheme is lower up to 32.51% than 'FDB with RIS' scheme, and higher up to 146.06% than the rest of three schemes. Furthermore, the beampatterns under different χ almost remain the same, which is because the variation of χ or noise power mainly affects SINR in communication, instead of sensing beampattern.

In conclusion, in this sub-section, we provide different parameter settings to evaluate their impact on both communication performance and sensing performance. From the simulation results, it can be observed that the sensing beampattern and communication UEs' SINR requirements can be satisfied by configuring suitable system parameters.

D. Tradeoff between Communication and Sensing

In this sub-section, we measure the tradeoff between communication and sensing by analyzing the SINR feasibility ratio, the average SINR of all the UEs over all the sub-carriers and the beampattern MSE. The beampattern MSE here refers to the mean square error of the beampatterns produced by the reference sensing matrix and covariance matrices of the designed beamformers,

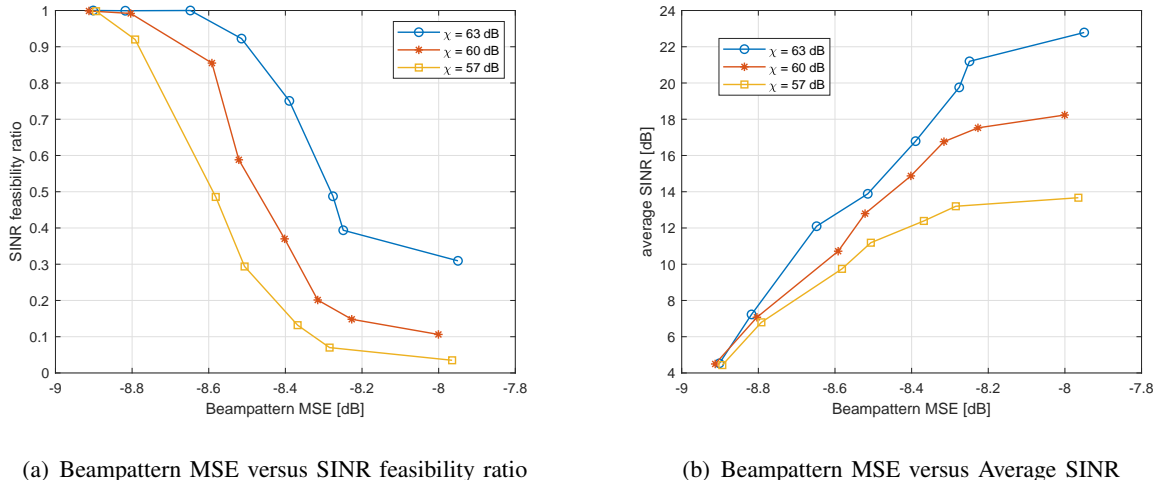


Fig. 10. Tradeoff between communication performance and sensing performance ($N_{RF} = 16$, $K = 4$, $R = 100$)

see Fig. 10. It can be observed that reaching a higher beampattern MSE corresponds to a lower SINR feasibility ratio and a higher average SINR, i.e., improving communication performance has a negative impact on sensing performance. For instance, in Fig. 10, we can see that under the case of $\chi = 57$ dB, reducing the beampattern MSE by 0.138 dB results in the increment by 0.1619 SINR feasibility ratio and the drop of 1.2 dB average SINR. Furthermore, given a better configuration, e.g. increasing the ratio of transmit power to noise power χ , a higher average SINR or a lower beampattern MSE can be obtained. For example, in Fig. 10(b), when χ is increased from 57 dB to 63 dB, up to 9.12 dB average SINR and -0.22 dB beampattern MSE are reached. Hence, different tradeoff between sensing and communication can be reached under different parameter configurations. For practical usage, the performances of communication and sensing are supposed to be weighed according to the required applications.

V. CONCLUSION

In this paper, we studied the potential of RISs in the OFDM JCAS system at mmWave bands. To maximize the performance of sensing and communication, we formulated an optimization model via the joint hybrid beamforming and phase shift design, in order to minimize the difference between the reference sensing matrix and the designed covariance matrices subject to the power and SINR constraints. By introducing an auxiliary variable and leveraging the penalty method, the manifold-based ADMM algorithm was proposed to solve the formulated non-convex problem. Simulation results demonstrated that our proposed scheme can improve

the SINR feasibility ratio up to 69.57% with the assistance of 200 RIS elements and saves power for optimizing sensing beampatterns. The tradeoff between sensing and communication is also discussed in the considered network. As a future work, we plan to model the mobility of targets/UEs and investigate its impact on the system performance.

REFERENCES

- [1] F. Liu, Y. Cui, C. Masouros, J. Xu, T. X. Han, Y. C. Eldar, and S. Buzzi, "Integrated sensing and communications: Towards dual-functional wireless networks for 6G and beyond," *IEEE Journal on Selected Areas in Communications*, vol. 40, no. 6, pp. 1728–1767, Jun. 2022.
- [2] C. Shi, F. Wang, M. Sellathurai, J. Zhou, and S. Salous, "Power minimization-based robust OFDM radar waveform design for radar and communication systems in coexistence," *IEEE Transactions on Signal Processing*, vol. 66, no. 5, pp. 1316–1330, Mar. 2018.
- [3] F. Liu, C. Masouros, A. Li, H. Sun, and L. Hanzo, "MU-MIMO communications with MIMO radar: From co-existence to joint transmission," *IEEE Transactions on Wireless Communications*, vol. 17, no. 4, pp. 2755–2770, Apr. 2018.
- [4] F. Liu, L. Zhou, C. Masouros, A. Li, W. Luo, and A. Petropulu, "Toward dual-functional radar-communication systems: Optimal waveform design," *IEEE Transactions on Signal Processing*, vol. 66, no. 16, pp. 4264–4279, Jun. 2018.
- [5] L. Chen, F. Liu, W. Wang, and C. Masouros, "Joint radar-communication transmission: A generalized Pareto optimization framework," *IEEE Transactions on Signal Processing*, vol. 69, pp. 2752–2765, May 2021.
- [6] F. Liu, Y.-F. Liu, A. Li, C. Masouros, and Y. C. Eldar, "Cramér-rao bound optimization for joint radar-communication beamforming," *IEEE Transactions on Signal Processing*, vol. 70, pp. 240–253, Dec. 2021.
- [7] X. Liu, T. Huang, N. Shlezinger, Y. Liu, J. Zhou, and Y. C. Eldar, "Joint transmit beamforming for multiuser MIMO communications and MIMO radar," *IEEE Transactions on Signal Processing*, vol. 68, pp. 3929–3944, Jun. 2020.
- [8] H. Hua, J. Xu, and T. X. Han, "Optimal transmit beamforming for integrated sensing and communication," *arXiv preprint arXiv:2104.11871*, 2021.
- [9] L. Pucci, E. Paolini, and A. Giorgetti, "System-level analysis of joint sensing and communication based on 5G new radio," *IEEE Journal on Selected Areas in Communications*, Mar. 2022.
- [10] Q. Zhang, Z. Li, X. Gao, and Z. Feng, "Performance evaluation of radar and communication integrated system for autonomous driving vehicles," in *IEEE INFOCOM 2021-IEEE Conference on Computer Communications Workshops (INFOCOM WKSHPS)*. IEEE, 2021, pp. 1–2.
- [11] A. Ali, N. Gonzalez-Prelcic, R. W. Heath, and A. Ghosh, "Leveraging sensing at the infrastructure for mmWave communication," *IEEE Communications Magazine*, vol. 58, no. 7, pp. 84–89, Jul. 2020.
- [12] J. Zhang, Y. Huang, J. Wang, X. You, and C. Masouros, "Intelligent interactive beam training for millimeter wave communications," *IEEE Transactions on Wireless Communications*, vol. 20, no. 3, pp. 2034–2048, Nov. 2020.
- [13] F. Liu and C. Masouros, "Hybrid beamforming with sub-arrayed MIMO radar: Enabling joint sensing and communication at mmWave band," in *ICASSP 2019-2019 IEEE International Conference on Acoustics, Speech and Signal Processing (ICASSP)*. IEEE, 2019, pp. 7770–7774.
- [14] Z. Cheng, Z. He, and B. Liao, "Hybrid beamforming design for OFDM dual-function radar-communication system," *IEEE Journal of Selected Topics in Signal Processing*, vol. 15, no. 6, pp. 1455–1467, Nov. 2021.
- [15] B. Wang, Z. Cheng, and Z. He, "Manifold optimization methods for hybrid beamforming in mmWave dual-function radar-communication system," *arXiv preprint arXiv:2111.15102*, 2021.

- [16] Z. Cheng, Z. He, and B. Liao, "Hybrid beamforming for multi-carrier dual-function radar-communication system," *IEEE Transactions on Cognitive Communications and Networking*, vol. 7, no. 3, pp. 1002–1015, Sept. 2021.
- [17] Z. Cheng and B. Liao, "QoS-aware hybrid beamforming and DOA estimation in multi-carrier dual-function radar-communication systems," *IEEE Journal on Selected Areas in Communications*, vol. 40, no. 6, pp. 1890–1905, Jun. 2022.
- [18] F. Liu, W. Yuan, C. Masouros, and J. Yuan, "Radar-assisted predictive beamforming for vehicular links: Communication served by sensing," *IEEE Transactions on Wireless Communications*, vol. 19, no. 11, pp. 7704–7719, Nov. 2020.
- [19] Q. Wu, S. Zhang, B. Zheng, C. You, and R. Zhang, "Intelligent reflecting surface-aided wireless communications: A tutorial," *IEEE Transactions on Communications*, vol. 69, no. 5, pp. 3313–3351, Jan. 2021.
- [20] M. Hua, Q. Wu, D. W. K. Ng, J. Zhao, and L. Yang, "Intelligent reflecting surface-aided joint processing coordinated multipoint transmission," *IEEE Transactions on Communications*, vol. 69, no. 3, pp. 1650–1665, Mar. 2020.
- [21] X. Ma, S. Guo, H. Zhang, Y. Fang, and D. Yuan, "Joint beamforming and reflecting design in reconfigurable intelligent surface-aided multi-user communication systems," *IEEE Transactions on Wireless Communications*, vol. 20, no. 5, pp. 3269–3283, Jan. 2021.
- [22] Q. Wu and R. Zhang, "Intelligent reflecting surface enhanced wireless network via joint active and passive beamforming," *IEEE Transactions on Wireless Communications*, vol. 18, no. 11, pp. 5394–5409, Nov. 2019.
- [23] G. Zhou, C. Pan, H. Ren, K. Wang, M. Di Renzo, and A. Nallanathan, "Robust beamforming design for intelligent reflecting surface aided MISO communication systems," *IEEE Wireless Communications Letters*, vol. 9, no. 10, pp. 1658–1662, Jun. 2020.
- [24] M. Zeng, E. Bedeer, O. A. Dobre, P. Fortier, Q.-V. Pham, and W. Hao, "Energy-efficient resource allocation for IRS-assisted multi-antenna uplink systems," *IEEE Wireless Communications Letters*, vol. 10, no. 6, pp. 1261–1265, Jun. 2021.
- [25] F. Fang, Y. Xu, Q.-V. Pham, and Z. Ding, "Energy-efficient design of IRS-NOMA networks," *IEEE Transactions on Vehicular Technology*, vol. 69, no. 11, pp. 14 088–14 092, Sept. 2020.
- [26] H. Xie, J. Xu, and Y.-F. Liu, "Max-min fairness in IRS-aided multi-cell MISO systems with joint transmit and reflective beamforming," *IEEE Transactions on Wireless Communications*, vol. 20, no. 2, pp. 1379–1393, Feb. 2021.
- [27] W. Ni, X. Liu, Y. Liu, H. Tian, and Y. Chen, "Resource allocation for multi-cell IRS-aided NOMA networks," *IEEE Transactions on Wireless Communications*, vol. 20, no. 7, pp. 4253–4268, Jul. 2021.
- [28] Z. Chu, P. Xiao, M. Shojafar, D. Mi, J. Mao, and W. Hao, "Intelligent reflecting surface assisted mobile edge computing for Internet of things," *IEEE Wireless Communications Letters*, vol. 10, no. 3, pp. 619–623, Nov. 2020.
- [29] Q. Wu and R. Zhang, "Joint active and passive beamforming optimization for intelligent reflecting surface assisted SWIPT under QoS constraints," *IEEE Journal on Selected Areas in Communications*, vol. 38, no. 8, pp. 1735–1748, Aug. 2020.
- [30] S. Buzzi, E. Grossi, M. Lops, and L. Venturino, "Foundations of MIMO radar detection aided by reconfigurable intelligent surfaces," *IEEE Transactions on Signal Processing*, vol. 70, pp. 1749–1763, Mar. 2022.
- [31] Z. Esmailbeig, K. V. Mishra, and M. Soltanalian, "IRS-aided radar: Enhanced target parameter estimation via intelligent reflecting surfaces," in *2022 IEEE 12th Sensor Array and Multichannel Signal Processing Workshop (SAM)*. IEEE, 2022, pp. 286–290.
- [32] X. Song, J. Xu, F. Liu, T. X. Han, and Y. C. Eldar, "Intelligent reflecting surface enabled sensing: Cramer-rao lower bound optimization," *arXiv preprint arXiv:2204.11071*, 2022.
- [33] J. Hu, H. Zhang, B. Di, L. Li, K. Bian, L. Song, Y. Li, Z. Han, and H. V. Poor, "Reconfigurable intelligent surface based RF sensing: Design, optimization, and implementation," *IEEE Journal on Selected Areas in Communications*, vol. 38, no. 11, pp. 2700–2716, Nov. 2020.
- [34] J. Hu, H. Zhang, K. Bian, M. Di Renzo, Z. Han, and L. Song, "Metasensing: Intelligent metasurface assisted RF 3D sensing

- by deep reinforcement learning,” *IEEE Journal on Selected Areas in Communications*, vol. 39, no. 7, pp. 2182–2197, Jul. 2021.
- [35] X. Shao, C. You, W. Ma, X. Chen, and R. Zhang, “Target sensing with intelligent reflecting surface: Architecture and performance,” *IEEE Journal on Selected Areas in Communications*, Mar. 2022.
- [36] X. Wang, Z. Fei, Z. Zheng, and J. Guo, “Joint waveform design and passive beamforming for RIS-assisted dual-functional radar-communication system,” *IEEE Transactions on Vehicular Technology*, vol. 70, no. 5, pp. 5131–5136, May 2021.
- [37] X. Wang, Z. Fei, J. Huang, and H. Yu, “Joint waveform and discrete phase shift design for RIS-assisted integrated sensing and communication system under Cramér-Rao bound constraint,” *IEEE Transactions on Vehicular Technology*, vol. 71, no. 1, pp. 1004–1009, Oct. 2021.
- [38] Z.-M. Jiang, M. Rihan, P. Zhang, L. Huang, Q. Deng, J. Zhang, and E. M. Mohamed, “Intelligent reflecting surface aided dual-function radar and communication system,” *IEEE Systems Journal*, vol. 16, no. 1, pp. 475–486, Feb. 2021.
- [39] S. Yan, S. Cai, W. Xia, J. Zhang, and S. Xia, “A reconfigurable intelligent surface aided dual-function radar and communication system,” in *2022 2nd IEEE International Symposium on Joint Communications & Sensing (JC&S)*. IEEE, 2022, pp. 1–6.
- [40] R. P. Sankar, B. Deepak, and S. P. Chepuri, “Joint communication and radar sensing with reconfigurable intelligent surfaces,” in *2021 IEEE 22nd International Workshop on Signal Processing Advances in Wireless Communications (SPAWC)*. IEEE, 2021, pp. 471–475.
- [41] T. Wei, L. Wu, K. V. Mishra, and M. B. Shankar, “Multiple IRS-assisted wideband dual-function radar-communication,” in *2022 2nd IEEE International Symposium on Joint Communications & Sensing (JC&S)*. IEEE, 2022, pp. 1–5.
- [42] R. Liu, M. Li, Y. Liu, Q. Wu, and Q. Liu, “Joint transmit waveform and passive beamforming design for RIS-aided DFRC systems,” *IEEE Journal of Selected Topics in Signal Processing*, May 2022.
- [43] X. Liu, H. Zhang, K. Long, M. Zhou, Y. Li, and H. V. Poor, “Proximal policy optimization-based transmit beamforming and phase-shift design in an IRS-aided ISAC System for the THz band,” *IEEE Journal on Selected Areas in Communications*, Mar. 2022.
- [44] F. Sahrabi and W. Yu, “Hybrid analog and digital beamforming for mmWave OFDM large-scale antenna arrays,” *IEEE Journal on Selected Areas in Communications*, vol. 35, no. 7, pp. 1432–1443, Jul. 2017.
- [45] Y.-P. Lin, “Hybrid MIMO-OFDM beamforming for wideband mmwave channels without instantaneous feedback,” *IEEE Transactions on Signal Processing*, vol. 66, no. 19, pp. 5142–5151, Aug. 2018.
- [46] Q. Wu and R. Zhang, “Beamforming optimization for wireless network aided by intelligent reflecting surface with discrete phase shifts,” *IEEE Transactions on Communications*, vol. 68, no. 3, pp. 1838–1851, Dec. 2019.
- [47] Z. Wang, L. Liu, and S. Cui, “Channel estimation for intelligent reflecting surface assisted multiuser communications: Framework, algorithms, and analysis,” *IEEE Transactions on Wireless Communications*, vol. 19, no. 10, pp. 6607–6620, Jun. 2020.
- [48] X. Liu, T. Huang, and Y. Liu, “Transmit design for joint MIMO radar and multiuser communications with transmit covariance constraint,” *IEEE Journal on Selected Areas in Communications*, vol. 40, no. 6, pp. 1932–1950, Jun. 2022.
- [49] P.-A. Absil and K. A. Gallivan, “Joint diagonalization on the oblique manifold for independent component analysis,” in *2006 IEEE international conference on acoustics speech and signal processing proceedings (ICASSP)*, vol. 5. IEEE, 2006, pp. 945–948.
- [50] N. Boumal, “An introduction to optimization on smooth manifolds,” *Available online, May*, vol. 3, 2020.
- [51] 3GPP, “TS 38.101-2 release 16,” Version 16.4.0, Jul. 2020.